https://doi.org/10.5194/acp-2019-793
Preprint. Discussion started: 21 October 2019

Atmospheric Chemistry and Physics Discussions
Open Access
EGU

Global Distribution and 14-Year Changes in Erythemal Irradiance, UV Atmospheric Transmission, and Total Column Ozone 2005 – 2018 Estimated from OMI and EPIC Observations

Jay Herman[1] Alexander Cede[2] Liang Huang[3] Jerald Ziemke[5]

Matthew Kowalewski[2], Karin Blank[4]

[1]University of Maryland Baltimore County JCET, Baltimore, Maryland USA

[2]SciGlob Instruments and Services, Ellicott City, Maryland, USA

[3]Science Systems and Applications, Lanham, Maryland, USA

[4]NASA Goddard Space Flight Center, Greenbelt, Maryland USA

[5]Morgan State University, GESTAR, Baltimore Maryland

Corresponding Author email: Jay.R.Herman@nasa.gov

https://doi.org/10.5194/acp-2019-793
Preprint. Discussion started: 21 October 2019

Atmospheric Chemistry and Physics Discussions

Abstract

Satellite data from the Ozone Measuring Instrument (OMI) and Earth Polychromatic Imaging Camera (EPIC) for ozone amount and scene reflectivity (mostly from clouds) are used to study changes and global distribution of UV erythemal irradiance in mW/m^2 $E(\zeta,\phi,z,t)$ and UV index ($E/25\ mWm^2$) over the Earth's surface as a function of latitude ζ, longitude ϕ, altitude z, and time t. OMI time series data starting in January 2005 to December 2018 are used to estimate 14-year changes in total column ozone TCO_3 and scene reflectivity at 105 specific land plus 77 ocean locations in the Northern and Southern Hemispheres. Estimates of changes in atmospheric transmission $T(\zeta,\phi,z,t)$ derived from cloud and haze reflectivity show almost no average 14-year change from $55^{O}S$ to $35^{O}N$ but show an increase from $40^{O}N$ to $60^{O}N$. This implies increased solar insolation at high northern latitudes that suggests positive feedback for global warming. TCO_3 has increased at a rate of 2% per decade for the latitudes between $60^{O}S$ to $10^{O}N$ changing to a decrease of 1% per decade between $40^{O}N$ to $60^{O}N$. The result is an average decrease in $E(\zeta,\phi,z,t)$ at a rate of 2% per decade in the Southern Hemisphere and an increase between $40^{O}N$ to $60^{O}N$. For some specific sites (latitudes from $55^{O}S$ to $45^{O}N$) there has been little or no change in $E(\zeta,\phi,z,t)$ for the period 2005 – 2018. Nearly half the sites show the effects of both short- and long-term cloud change as well as total column ozone change. Synoptic EPIC data from the sunlit Earth are used to derive ozone and reflectivity needed for global images of the distribution of $E(\zeta,\phi,z,t)$ from sunrise to sunset centered on the Americas, Europe-Africa, and Asia. EPIC data are used to show the latitudinal distribution of $E(\zeta,\phi,z,t)$ from the equator to 75^{O} for specific longitudes. Dangerously high amounts of erythemal irradiance ($12 <$ UV index < 18) are found for many low latitude and high-altitude sites (e.g., San Pedro, Chile (2.45 km), La Paz, Bolivia (3.78 km). Lower UV indices at some equatorial or high-altitude sites (e.g., Quito, Ecuador) are moderated by the presence of persistent cloud effects. High UVI levels (UVI > 6) are also found at most mid-latitude sites during the summer months. High levels of UVI are known to lead to health problems (skin cancer and eye cataracts) with extended unprotected exposures as shown in the extensive health statistics maintained by Australian Institute of Health and Welfare and the United States National Institute of Health National Cancer Institute.

https://doi.org/10.5194/acp-2019-793
Preprint. Discussion started: 21 October 2019

Atmospheric Chemistry and Physics Discussions

1 Introduction

Calculated or measured amounts of UV radiation reaching the Earth's surface can be used as a proxy to estimate the effects of changing ozone and cloud cover on human health. High levels of UV irradiance are known to affect the incidence of skin cancer (Findlay 1928, Diffey, 1987, Strom and Yamamura, 1997) and the development of eye cataracts (Ambach and Blumthaler, 1993; Abraham et al., 2010; Roberts, 2011, Australian Institute of Health and Welfare, 2016, Howlander et al., 2019). The UV response function (action spectra) for the development of skin cancer and eye cataracts are different (Herman, 2010), but the effects are highly correlated. Similar correlations exists for other action spectra (e.g., plant growth, vitamin D production, and DNA damage action spectra) involving the UV portion of the solar spectrum. Because of these correlations, this paper will only estimate erythemal (skin reddening) effects. To obtain standardized results, we use a weighted UV spectrum based on the CIE-action (Commission Internationale de l'Eclairage) spectrum suggested by McKinlay and Diffey (1987) to estimate the erythemal effect of UV radiation incident on human skin. erythemal irradiance (E) is usually measured or calculated in energy units (mW/m^2) reaching the Earth's surface after passing through atmospheric absorbing and scattering effects from ozone, aerosols, and clouds for the wavelength range 300 – 400 nm. A fast algorithm (Herman, 2010) for calculating E and other action spectra was developed based on calculations using the scalar TUV radiative transfer program (Madronich , 1993a; 1993b; Madronich and Flocke, 1997). The fast algorithm was extended to include the effect of increasing E with altitude (Herman et al., 2018) as applied to the synoptic measured amounts of ozone, clouds and aerosols obtained by the EPIC (Earth Polychromatic Imaging Camera) instrument onboard the DSCOVR (Deep Space Climate Observatory) spacecraft orbiting about the Earth-Sun Lagrange-1 gravitational balance point (Herman et al., 2018; Marshak et al., 2018).

This paper presents calculated noontime $E(\zeta,\phi,z,t)$ time series and least squares LS linear trends from 2005 – 2018 for 105 globally distributed locations at different latitudes ζ, longitudes ϕ, altitudes z, and time t (in years) most of which are centered on heavily populated areas such as New York City, Seoul Korea, Buenos Aires, etc. (see Tables 1, 2, and 3 and an extended table A4 for 105 land sites in the Appendix) based on measurements of the relevant parameters from OMI (Ozone Monitoring Instrument) onboard the AURA spacecraft. An additional 77 locations in the Atlantic and Pacific Ocean for a range of latitudes are also discussed. OMI satellite measurements were selected because OMI has the longest continuous well calibrated UV irradiance time series from a single instrument with global coverage and moderate spatial resolution (13x24 km^2 at its nadir view). The derived numerical algorithms used for the calculations are given in the Appendix. Estimates are given of 14-year latitude dependent changes in atmospheric transmission $T(\zeta,\phi,z,t)$ (mostly from change in cloud reflectivity), changes on total column ozone $TCO_3(\zeta,\phi,z,t_O)$, and changes in erythemal irradiance $E(\zeta,\phi,z,t_O)$. To augment the specific locations selected for time series analysis, synoptic sunrise to sunset estimates of $E(\zeta,\phi,z,t_O)$ are derived from EPIC measurements of the illuminated Earth at several Greenwich Mean Times t_O with a spatial resolution of 18x18 km^2 at the spacecraft nadir view for various longitudes centered on the Americas, Europe-Africa, and Asia.

https://doi.org/10.5194/acp-2019-793
Preprint. Discussion started: 21 October 2019

Atmospheric Chemistry and Physics Discussions

2 Erythemal Time Series and LS Linear Trends

Total column ozone amounts TCO_3 and 340 nm Lambert Equivalent Reflectivity LER (converted to transmission T(ζ,φ,z,t)) are retrieved from spectrally resolved irradiance measurements (300 – 550 nm) obtained from OMI for the entire Earth. OMI data are filtered to remove measurements obtained from portions of the CCD detector affected by the "row anomaly" (Schenkeveld et al., 2017). OMI is a polar orbiting side viewing satellite instrument (2600 km width on the surface) onboard the AURA spacecraft that provides near global coverage (nadir resolution field of view 13 km x 24 km) once per day from a 90-minute polar orbit with an equator crossing time of approximately 13:30 local solar time (LST) (Levelt et al., 2018). Because of OMI's simultaneous side-viewing capability, there are occasionally a 2nd or 3rd data points (±90 minutes) from adjacent orbits at higher latitude locations. This study uses column ozone amounts (in Dobson units DU, 1 DU = 2.687×10^{16} molecules/cm^2) and 340 nm Lambert equivalent reflectivity LER (Herman et al., 2009) (LER is in reflectivity units, 0<RU<100) data organized in gridded form for the entire sunlit Earth every 24 hours. Ozone and reflectivity data (2005 – 2018) at a resolution of 1^{O} x 1^{O} are available in ASCII format from https://avdc.gsfc.nasa.gov/pub/tmp/OMI_Daily_O3_and_LER/ for latitude ζ, longitude φ, and time t (in fractional years) in order to estimate noontime E(ζ,φ,z,t). The LER data has been corrected for instrument drift by requiring that the LER values over the Antarctic high plateau region remain constant over 14 years. The LER calibration correction permits 14-year linear LS trends to be estimated. A gridded 1^{O} X 1^{O} Version 8.5 ozone product is available from https://avdc.gsfc.nasa.gov/pub/DSCOVR/OMI_Gridded_O3/. Site specific time series are generated from the 1^{O}x1^{O} degree latitude by longitude files. The numerical algorithm (see Appendix) for erythemal analysis is applied for the Northern and Southern Hemispheres and equatorial region and discussed in separate sections of this paper.

Least squares linear LS trends for E(ζ,φ,z,t) computed from the original OMI TCO_3(ζ,φ,z,t) and LER(ζ,φ,t) time series having non-uniform temporal sampling give incorrect trends or slopes S(ζ,φ), given in percent change per year. Instead, LS linear trends for 105 sites (Appendix Table A4) are computed from uniform temporal density (UTD method) time series based on interpolation using 2.5 times the point count of the original time series. Further increases in interpolated point count N do not change the S(ζ,φ) significantly. However, the interpolated time series results yield an incorrect estimated standard deviation, since σ(ζ,φ) decreases as $N^{-0.5}$. Better standard deviations σ(ζ,φ) are computed from the original non-uniform times series, which represents the scatter caused by the OMI non-uniform sampling, intrinsic measurement noise, and atmospheric variation. Error bars shown in the various graphs are statistical and do not represent possible small systematic calibration drifts in determining TCO_3 from the OMI instrument data (see section 3.5).

A standard multivariate (MV) method (Guttman, 1982) was used to check the UTD method for both trends S(ζ,φ) and trend uncertainties σ(ζ,φ). The results of the MV method (appendix Table A5) comparison are based on analyzing two time series, E(t) and O_3(t), for LS linear trends at each site and using daily means as a reference value to estimate percent change per year. The results show that the UTD method and the MV method approximately agree for S(ζ,φ) and σ(ζ,φ) for both E(t) and

$TO_3(t)$. Table A5 illustrates comparisons of $S(\zeta,\phi)$ and $\sigma(\zeta,\phi)$ from 5 sites showing that either method may be used with comparable results. All subsequent calculations use the UTD method.

Erythemal Irradiance LS linear trends were also estimated from time series where the annual seasonal solar zenith angle dependence is removed. The LS linear trend results were almost the same, but the estimated deseasonalized error was about half the original error estimate. The original fitting error estimates $\sigma(\zeta,\phi)$ are used.

2.1 Northern Hemisphere

Figure 1 and Table 1 show erythemal irradiance $E(\zeta,\phi,z,t)$ time series (mW/m^2) and their LS linear trends (in percent change per year along with their 1σ standard deviation) at six sites with various altitudes z within the United States from 2005 – 2018 (14 annual cycles). The right-side axis shows the proportional values of the standard UV index, UVI = E/25 mW/m^2. Erythemal time series are truncated to start and stop at the same point in their 14-year annual cycles (1 January 2014 to 31 December 2018). The time series depicted in Fig.1 are non-uniform in time with significant gaps between some adjacent points. In all cases the gaps are small enough to properly represent the SZA dependence of the erythemal irradiance. Of the six United States sites listed in Table 1, rural Georgia (also Atlanta, GA), Tampa, FL, and Honolulu HI have 2σ significant trends of 0.3%/Year, -0.24%/Year, and -0.27%/Year (Table 1). These sites have small changes in ozone amount but significant changes in cloud + haze transmission, 0.15, -0.25, and -0.24 %/Yr, respectively. Of human health interest are the maximum values that occur during the summer months when the solar zenith angle is near a local minimum reducing the slant column ozone absorption and Rayleigh scattering for clear-sky days. In terms of the UV index, a value of 6 will produce significant skin reddening in light skinned people in about an hour of unprotected exposure (Diffey, 1987; 2018; Italia and Rehfuess, 2012). In local shade, there is reduced but significant exposure from atmospheric scattering (Herman et al., 1999) with the shorter more damaging wavelengths scattering the most. For sites with extremely high UVI (10 – 18) even shaded areas can produce significant exposure from scattered UV. Table 1 shows the 14-year average maximum UVI and the 14-year average UVI.

For the mid-latitude site, Greenbelt, Maryland 39^{O}N, summer values between 8 and 9 are frequently reached with a few days reaching 10 and 1 day reaching 11 on 6 June 2008. The cause was a low ozone value of 283 DU on a clear-sky day compared to more normal values between 310 and 340 DU. The basic annual cycle follows the solar zenith angle (SZA) with the minimum angle occurring during the summer solstice. For Greenbelt, MD, this angle is approximately 39 – 23.3 = 15.7^{O}. Sites with fewer clouds plus haze and closer to the equator have higher maximum UV-index values, 12 for White Sands, NM and 11 for Tampa, Florida. Results corresponding to Fig. 1A are summarized in Table 1 (see also appendix Table A4). The last 2 columns give the estimated slope of a linear LS fit (UTD method) to each time series and the standard deviation (σ). Graphs summarizing the 105-site Table A4 are given in section 3.5, which show the expected change in UVI for decreasing latitude. Since the purpose is estimating changes in E from all causes, the effects of the quasi-biennial oscillation (QBO) and solar cycle are not removed from the ozone time series.

https://doi.org/10.5194/acp-2019-793
Preprint. Discussion started: 21 October 2019

Atmospheric Chemistry and Physics Discussions

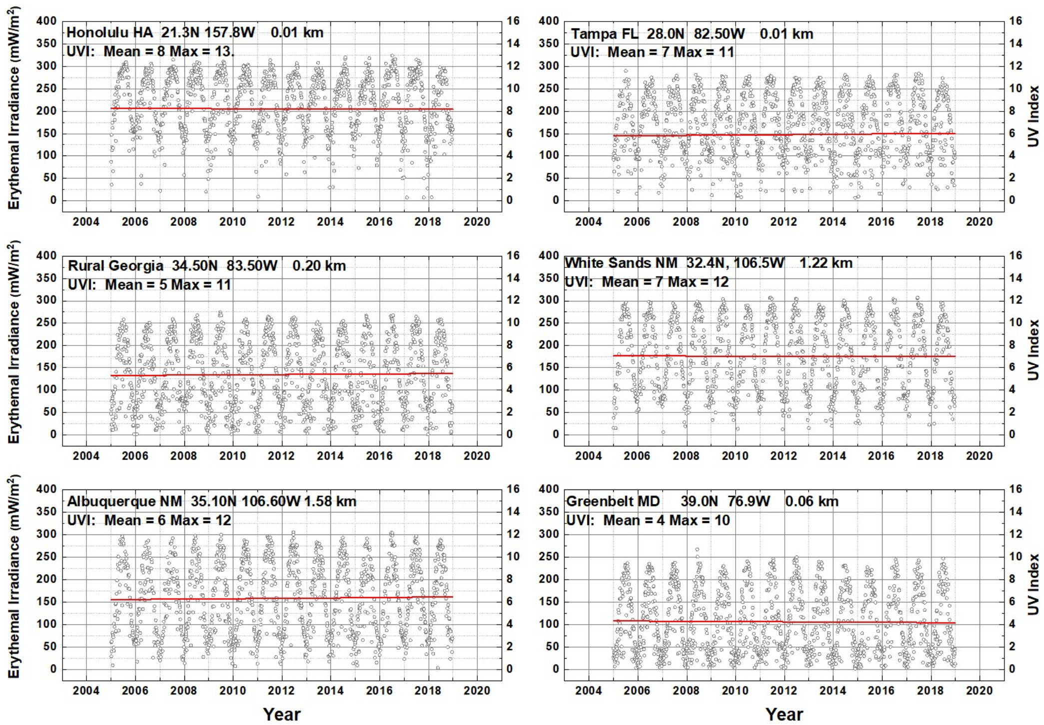

Fig. 1A Erythemal Irradiance E(ζ,ϕ,z,t) at six selected sites from Table A1 distributed within the United States. The red line is the linear fit to each of the time series. Also listed are the 14-year UVI average maximum and average values (UVI = E/25) (See table 1).

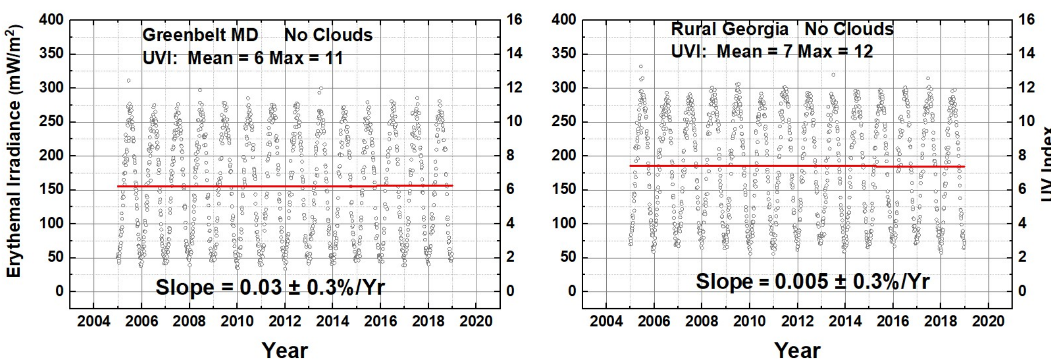

Fig. 1B Two sites from Fig. 1A, Greenbelt, Maryland and Rural Georgia, with the effect of clouds removed (i.e., T=1)

https://doi.org/10.5194/acp-2019-793
Preprint. Discussion started: 21 October 2019

Table 1 Locations in the United States (Errors are 1σ)

Location	Lat	Lon	Alt	UVI	UVI	←------------------	Trends (%/Year)			------------------→	
	Deg	Deg	km	Avg	Max	ERY	±Error	Ozone	±Error	Trans	±Error
Albuquerque, NM	35.1	-106.6	1.58	6	12	0.18	0.11	-0.11	0.02	0.33	0.05
Greenbelt, MD	39	-76.9	0.06	4	10	-0.19	0.15	-0.13	0.03	-0.1	0.08
*Honolulu, HI	21.3	-157.8	0.01	9	12	-0.27	0.06	-0.02	0.01	-0.24	0.03
*Rural GA	34.5	-83.5	0.2	5	10	0.3	0.12	-0.08	0.02	0.15	0.07
*Tampa, FL	28	-82.5	0.01	7	11	-0.24	0.09	-0.03	0.02	-0.25	0.06
White Sands, NM	32.4	-106.5	1.22	7	12	-0.07	0.1	-0.07	0.02	-0.06	0.04

*Means 2σ trend significance for erythemal change

When $\zeta(t)$ = SZA and T(t) = transmission are held constant for calculating $E(\zeta(t), O_3(t), T(t))$, a 1% change in total column ozone amount $\Omega = TCO_3$ produces approximately a 1.2% change in erythemal irradiance. The exact amount of change is dependent on the SZA selected (Eqn. 2). The values for O_3 and T change (%/Year) are given in Table 1, which shows that a significant amount of the erythemal irradiance change over 14 years is caused by changes in cloud cover.

A numerical solution of the radiative transfer equation for the erythemal action spectrum can be approximated by the functional form in Eq. 1 (see the appendix Eqn. A4), where the cloud + scattering aerosol transmission $T = (1-LER)/(1-R_G)$, $(1 > T > 0)$, ζ = SZA, and R_G = reflectivity of the surface (an average of about 0.05) in the absence of snow or ice. This form gives an improved version of the Radiation Amplification Factor $R(\zeta)$ that is independent of TCO_3 (Herman, 2010).

$$E(\Omega,\zeta) = U(\zeta)\,(\Omega/200)^{-R(\zeta)}\;T \qquad (1)$$

For a given time, t, the sensitivity to changes in Ω and θ

$$\frac{dE}{E} = -R(\xi)\frac{d\Omega}{\Omega} + \frac{dT}{T} + \frac{dU(\xi)}{U(\xi)} - R(\xi)\ln\left(\frac{\Omega}{200}\right)\frac{dR(\xi)}{R(\xi)} \qquad (2)$$

Where $dU(\zeta) = U(\zeta + d\zeta) - U(\zeta)$ and $dR(\zeta) = R(\zeta + d\zeta) - R(\zeta)$

For $\zeta = 0$, $R(0) = 1.2$ and $R(\zeta)$ gradually decreases to 0.85 for $\zeta = 80^{O}$ (Herman, 2010 and Appendix Fig. A1). SZA variation is the primary anti-correlated driver for the annual cycle of erythemal irradiance (Fig. 1) at each location except when there is heavy cloud cover. The cycle for $E(\zeta,\phi,z,t)$ is perturbed by the smaller effect of short-term changes in ozone amount and reflectivity that are shifted in phase from $\zeta(t)$. The result is that the separately estimated 14-year linear trends for T and Ω may not be simply additive. For example, for the Rural Georgia site Fig. 1, the erythemal trend is statistically significant at 0.3 ± 0.12 %/Yr. Contributing factors

https://doi.org/10.5194/acp-2019-793
Preprint. Discussion started: 21 October 2019

are the cloud transmission function T(t) trend 0.15 ± 0.07 %/Year, and small Ω(t) trend -0.08 ± 0.02 %/Year. In Fig. 1B, the E(ζ,ϕ,z,t) trend for Rural Georgia without clouds is 0.005 ± 0.3 %/Yr. The linearly combined trend is 0.15+0.08 = 0.23 ± 0.07 %/Yr, which overlaps the erythemal trend error estimate.

For Greenbelt, the erythemal LS linear change in E(t) is -0.19 ± 0.15 %/Yr, while the ozone change is –0.13 ± 0.03 %/Yr and transmission change is -0.1 ± 0.08 %/Yr. Within overlapping error estimates, these changes are consistent. The trend for the no cloud case (Fig. 1B) is 0.03 ± 0.3 %/Yr, but the error estimate is large enough to include the ozone change of -0.13%/Yr. If the figures for Greenbelt with (Fig. 1A) and without clouds (Fig. 1B) are compared, the effect of cloud cover is seen in the reduction of the maximum and mean UVI values and in the strong reduction during the winter months when cloud cover is frequent. The rural Georgia time series also shows a winter cloud effect that is smaller than for Greenbelt. As expected, White Sands and Albuquerque, New Mexico show little winter cloud effects.

Figure 2A shows the latitudinal distribution, 0^O to 80^ON, of erythemal irradiance estimated from the synoptic EPIC measurements on a line of longitude passing through San Francisco, CA at 19:37 GMT or 11:37 PST. The main driver of the decrease in E(ζ) from the equator toward the poles is the increased optical path from increasing SZA(ζ) and increasing TCO_3(ζ) absorption. The smaller structure near 10^O, 21^O, 37^ON is caused by small amounts of cloud cover reducing the transmission T(ζ). This day, 30 June 2017, near the 22 June solstice was selected based on the data from DSCOVR-EPIC showing that there were few clouds present in the scene (Fig.2B) with T near 1. All the E(ζ) estimates in Fig. 2A are at or near sea level and yield a maximum UVI = 12 near 13^ON latitude. Similarly, Fig. 2C shows the latitudinal distribution of E(ζ) for the line of longitude passing near Greenwich England at 0.25^OE. E(ζ) is reduced because of cloud cover starting at 40^ON in addition to the increasing ozone absorption at higher latitudes. The accompanying images in Figs. 2B and 2D show the distribution of E(ζ) and the location of significant cloud cover.

https://doi.org/10.5194/acp-2019-793
Preprint. Discussion started: 21 October 2019

Atmospheric Chemistry and Physics
Discussions

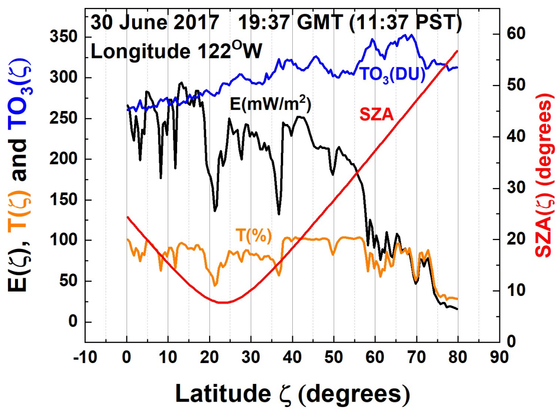

Fig. 2A Latitudinal distribution of E(ζ) and its contributing factors, TC(O_3), T, and SZA for a line of longitude passing through San Francisco, CA.

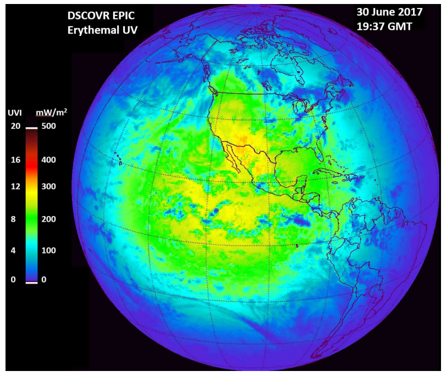

Fig. 2B Global distribution of E(ζ,ϕ) from DSCOVR EPIC data on 30 June 2017 19:17 GMT when there were few clouds.

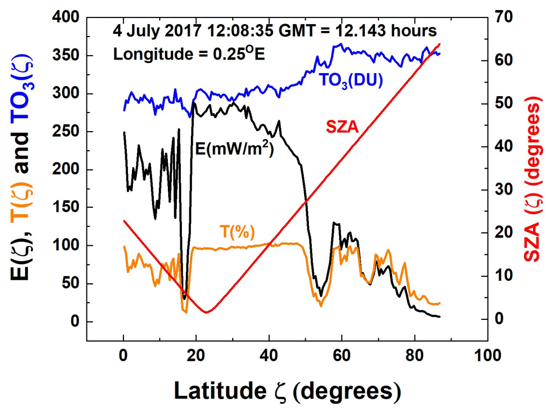

Fig. 2C Latitudinal distribution of E(ζ,ϕ,z,t) and its contributing factors, TC(O_3), T, and SZA for a line of longitude passing near Greenwich England

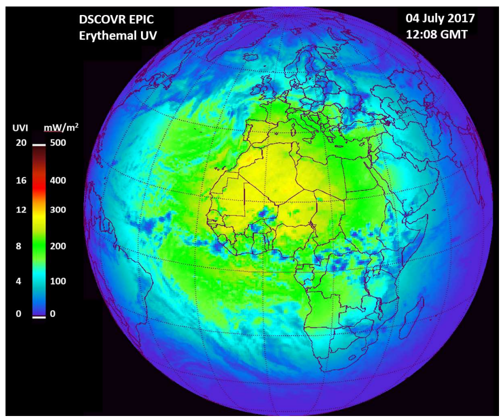

Fig. 2D Global distribution of E(ζ,ϕ) from DSCOVR EPIC data on 04 July 2017 12:08 GMT.

2.2 Equatorial Region

Four selected equatorial sites (Fig. 3 and Table 2) show very different behavior compared to mid-latitude sites shown in Fig. 1 and listed in Table 1. The average E(ζ,ϕ,z) is higher (UVI=9) for the near sea level site in Manaus, Brazil than the populated city of Quito, Ecuador at 2.9 km altitude (mean UVI= 6). The lower average Quito value is caused by the presence of additional cloud cover (mean transmission <T> = 0.34) compared to Manaus (mean

https://doi.org/10.5194/acp-2019-793
Preprint. Discussion started: 21 October 2019

transmission <T> = 0.68). The effect of high altitude, 5.2 km, is seen for the Mt. Kenya site having UVI values up to 18.

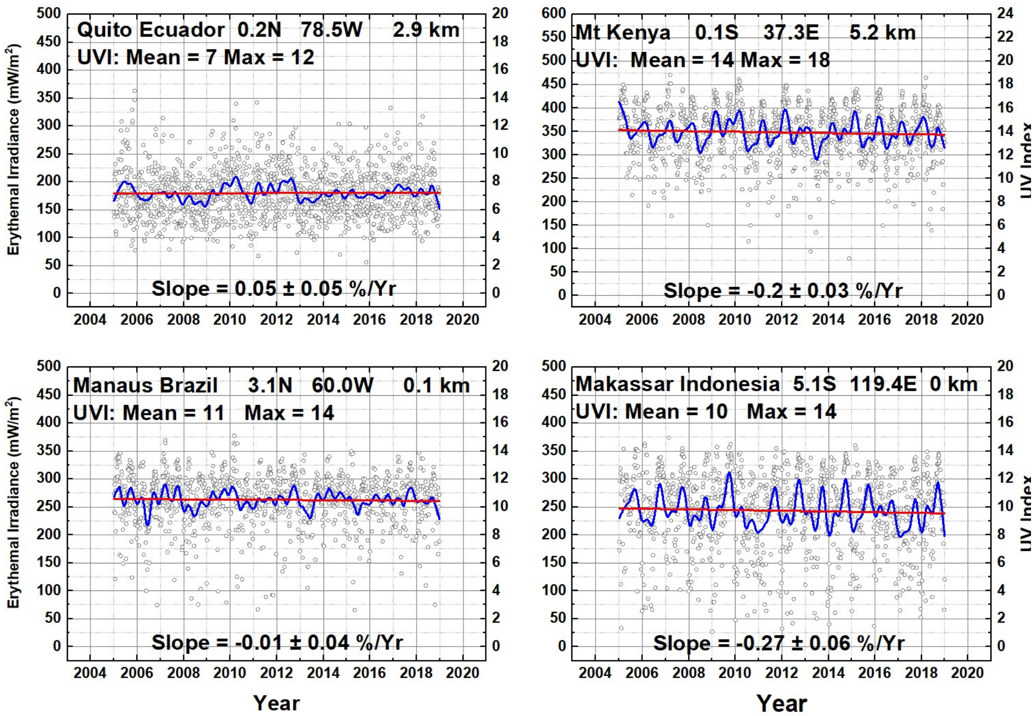

Figure 3. Four sites located close to the equator. Mt Kenya at 0.1°S, Quito Ecuador 0.2°N, Makassar Indonesia 5.1°S, Manaus Brazil 3.1°N. The blue lines are a Lowess(0.04) fit (approximately 6 month LS running average). Lowess(f) is Locally Weighted least squares fit to a fraction f of the data points, (Cleveland, 1981).

Figure 4A shows the effect of altitude causing an increase in clear-sky E(ζ,ϕ,z,t) for Quito (2.9 km) compared to Manuas (0.1 km) plus a small difference in average TCO_3 (2%) between the two locations. Without clouds, both sites show a double peak corresponding to SZA = 0^O twice a year near the March and September equinoxes. Figure 4B has an expanded time scale for 2005 showing the double peak for Quito and the strong effect of clouds in the region. The average cloud-free value for Quito has a UVI = 15 and a maximum UVI = 19. The minimum cloud-free value is UVI = 13 instead of 3 when cloud cover is included. The cloud effect is less at inland sites at Manaus Brazil and Mt Kenya, and even at the coastal Makassar, Indonesia site. The 20 DU variation in TCO_3 causes the autumn peak in E(ζ,ϕ,z,t) without clouds to be smaller than the spring peak.

https://doi.org/10.5194/acp-2019-793
Preprint. Discussion started: 21 October 2019

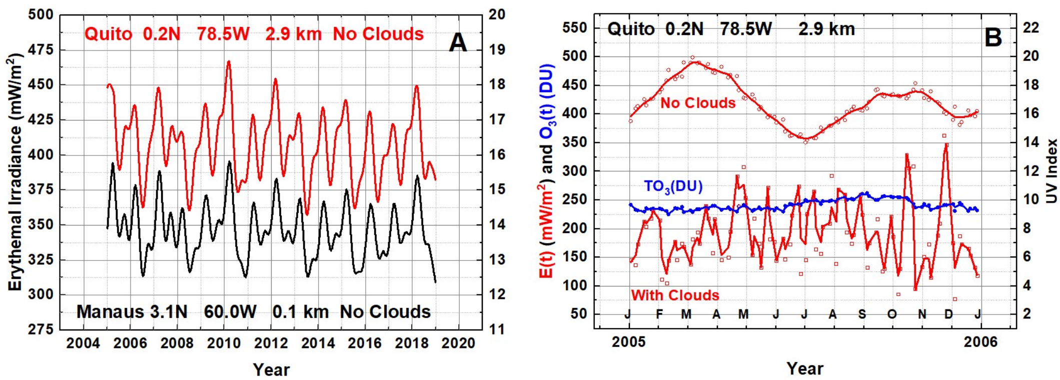

Fig. 4 Panel A: A two week running average of cloud-free E(ζ,ϕ,z,t) corresponding to the data in Fig. 3A for Quito Ecuador and Manaus Brazil showing the effect of height and a small difference in average ozone amount. Panel B: An temporal expansion for one year (2005) of E(ζ,ϕ,z,t) estimates for Quito showing the double peak as a function of minimum SZA near the equinoxes in the absence of clouds that is masked when clouds are included. The blue line shows the 20 DU variation in ozone between March and September.

Table 2 Summary of Equatorial Sites (Errors are 1σ)

Location	Lat	Lon	Alt	UVI	UVI	←------------------ Trends (%/Year) ------------------→					
	Deg	Deg	km	Avg	Max	ERY	±Error	Ozone	±Error	Trans	±Error
*Mt Kenya, KE	0.13	37.3	5.2	14	18	-0.2	0.03	0.17	0.01	0.03	0.03
Quito, EC	0.18	-78.5	2.85	7	12	0.05	0.05	0.17	0.01	0.28	0.05
*Makassar, ID	-5.13	119.4	0.01	10	14	-0.27	0.06	0.19	0.01	-0.05	0.06
Manaus, BR	3.12	-60	0.09	11	14	-0.01	0.04	0.16	0.01	0.24	0.04

The calculations based on 1^{O} x 1^{O} (100x100 km^2) spatial resolution can obscure an important health related result. In Quito, there are frequent localized clear periods when the UV index can rise to the clear-sky values (13<UVI<18), an increase of about 10, which are a serious health threat for skin cancer and cataracts all year. In Honolulu (21.3^{O}), the double peak in E(ζ,ϕ,z,t) is not significantly separated in time (15 days) to be easily discernable, but it causes the slightly different shape in the annual cycle (Fig. 1). In general, equatorial sites have increased E(ζ,ϕ,z,t) compared to higher latitudes because of both lower SZA values and less ozone near the equator giving reduced UV absorption and increased E(ζ,ϕ,z,t).

Two of the four equatorial sites in Fig. 3 show significant linear trends (Makassar Indonesia, and Mt Kenya, Kenya with the Makassar Indonesia site showing the largest linear trend, -0.27 ± 0.06%Year. For Makassar, ozone is increasing at a rate of 0.19 ± 0.01 %/Year, which by itself would cause UVI to decrease at a rate of -0.23 ± 0.01 %/Year. Atmospheric

https://doi.org/10.5194/acp-2019-793
Preprint. Discussion started: 21 October 2019

transmission (Fig. 4B) is slightly decreasing a rate of -0.05 ± 0.06%/Year causing E(ζ,ϕ,z,t) to have a net decrease. When combined (Fig. 4), the net effect is dominated by the increase in ozone. In the absence of clouds, the percent decrease in ozone amount causes an increase in E(ζ,ϕ,z,t) at approximately a 1.2:1 ratio. Figure 4B shows the approximate anti-correlation between ozone amounts and E(ζ,ϕ,z,t) for Quito and Manaus. This is modified by the six-month shifting of the sub-solar point (SZA = 0). When all four periodic and quasi-periodic effects are combined, the result is the aperiodic function shown in Fig.4B for Quito, Ecuador. Similar analysis applies for Manaus, Brazil located near the Amazon River, which is dominated by variable cloud driven atmospheric transmission, but less than for Quito, Ecuador. The other two equatorial sites Makassar, Indonesia and Mt. Kenya, Kenya have smaller cloud effects and show periodic structures driven by SZA and ozone absorption.

2.3 Southern Hemisphere

Time series for the Southern Hemisphere are represented by six sites shown in Fig. 5 ranging in latitude and altitude (12.5^{O} to 54.8^{O} and 0 to 2.5 km). All the sites have a clear annual cycle compared with the Northern Hemisphere sites. The maxima occur in January and minima in June. Of these, Darwin Australia is within the equatorial zone (12.5^{O}S) and shows the double peak structure with peaks separated by about 85 days. The site furthest from the equator, Ushuaia (54.8^{O}S) has the lowest UVI peak value of 9.6 (14-year average maximum UVI = 8) and a lowest 14-year minimum average UVI=2. Occasionally the Antarctic ozone depletion region passes over Ushuaia giving rise to increased UV amounts, but these episodes (September – October) do not correspond to the maximum UVI values that occur with the minimum SZA in January. For the sites in Fig. 5, the populated site San Pedro de Atacama has the largest UVI maximum (18) and average (11), since it is at moderate altitude (2.5 km) and is located at the southern edge of the equatorial zone (23^{O}) with a relatively clear cloud-free atmosphere. More than half of the days each year have 10 < UVI < 18. This maximum UVI is higher than for equatorial Darwin Australia, UVI < 15.5. The frequent June minima for Darwin are UVI=8 with occasional days at UVI=2 caused by clouds, while the almost cloud-free San Pedro de Atacama has minima of UVI=4 corresponding to a June noon SZA = 46^{O} compared to Darwin June SZA = 36^{O}. Both sites have about the same typical TCO_3, 255 DU.

Previous estimations of erythemal irradiance from measurements (1997-1999) and calculations (using Total Ozone Mapping Spectrometer data) at Ushuaia (Cede et al., 2002; 2004) shows very similar values with a UVI < 1 in the winter (June) and with values up to 8 with an occasional point reaching 10 during the summer (January) and for Buenos Aires with values of UVI from 1-2 in the winter and up to 12-13 in the summer. These values approximately agree with those in Table 3. The Cede et al. (2004) results for 8 sites also include a higher altitude equatorial site, La Quiaca, AR (22.1^{O}S), at 3.46 km altitude, having summer values up to

https://doi.org/10.5194/acp-2019-793
Preprint. Discussion started: 21 October 2019

Atmospheric Chemistry and Physics Discussions

UVI = 20. The corresponding calculated estimates using OMI data (2005-2018) also have the maximum UVI = 20 occurring in 2010 with a 14-year average maximum of UVI=18 (Table 3). La Quiaca has decreasing E(t) caused by increasing cloudiness and increasing TCO_3.

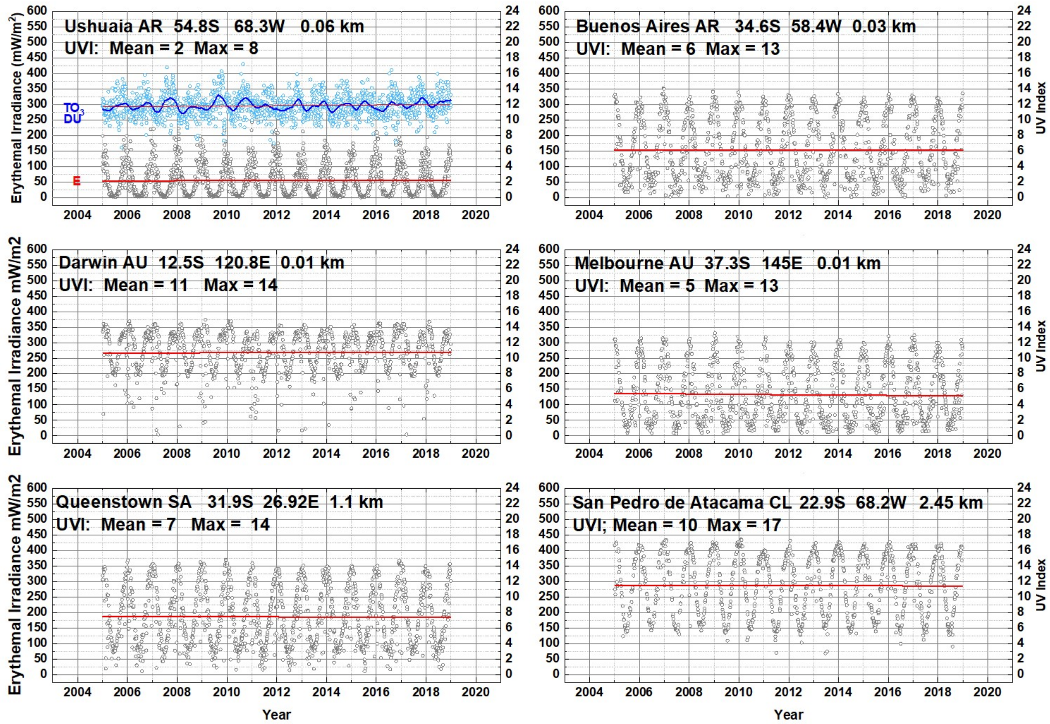

Fig. 5: Six sites in the Southern Hemisphere including estimates of the trends for E(ζ,ϕ,z,t), $TC(O_3)$, and the atmospheric transmission T caused by clouds and haze. The $TC(O_3)$ time series (blue) is shown for Ushuaia

https://doi.org/10.5194/acp-2019-793
Preprint. Discussion started: 21 October 2019

Table 3 Summary for 7 Southern Hemisphere Sites (Errors are 1σ)

Location	Lat	Lon	Alt	UVI	UVI	←------------------ Trends (%/Year) ---------------→					
	Deg	Deg	km	Avg	Max	ERY	±Error	Ozone	±Error	Trans	±Error
Darwin, AU	-12.5	120.8	0.01	11	14	0.04	0.05	0.12	0.01	0.15	0.04
La Quiaca, AR	-22.1	-65.6	3.46	12	18	-0.15	0.07	0.09	0.01	-0.12	0.04
San Pedro CL	-22.9	-68.2	2.45	11	17	-0.0	0.08	0.15	0.01	0.06	0.02
Queenstown, SA	-31.9	26.92	1.1	7	14	-0.1	0.11	0.16	0.01	0.01	0.05
Buenos Aires, AR	-34.6	-58.4	0.03	6	13	-0.2	0.14	0.08	0.02	-0.1	0.07
Melbourne, AU	-37.3	145	0.01	5	13	-0.4	0.15	0.25	0.02	-0.24	0.06
Ushuaia AR	-54.8	-68.3	0.06	2	8	0.01	0.2	0.18	0.03	0.05	0.07

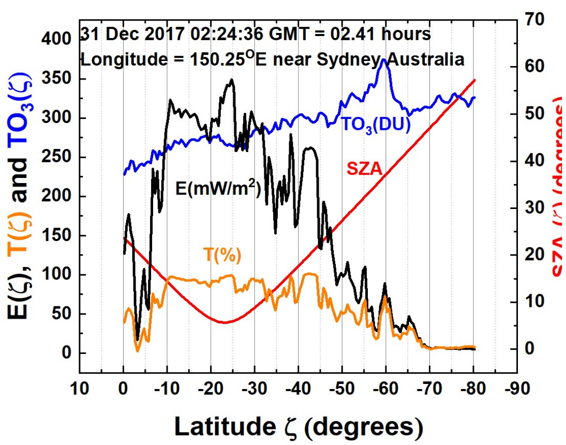

Fig. 6A Latitudinal distribution of E(ζ,ϕ,z,t) and its contributing factors, TC(O_3), T, and SZA for a line of longitude passing near Sydney, Australia

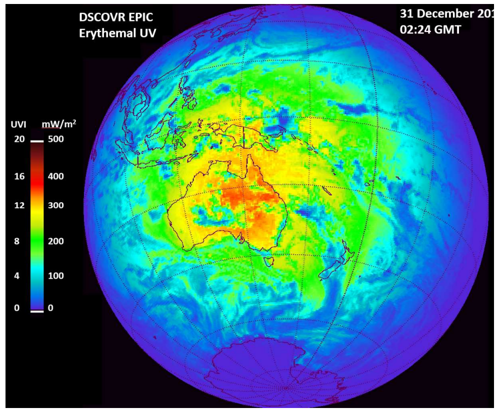

Fig. 6B Global distribution of E(ζ,ϕ) from DSCOVR EPIC data on 31 December 2017 02:24:36 GMT.

Figure 6A shows the latitudinal distribution, 0^O to 80^OS, of erythemal irradiance on a line of longitude passing near Sydney Australia at 02:24:36 GMT or 1:24 NSW (New South Wales). The main driver of the decrease in E(ζ) from the equator toward the poles is the increased optical path from increasing SZA(ζ) and the increasing TCO_3(ζ). The smaller structures near 40^O, 50^O, 60^OS are caused by small amounts of cloud cover reducing the transmission T(ζ). The 31 December day near the solstice was selected based on data from DSCOVR-EPIC showing that there were few clouds present over Australia (Fig.6B). All the E(ζ) estimates in Fig. 6A are near sea level with a maximum UVI = 14 near 25^OS latitude. Figure 6B shows the distribution of high E(ζ,ϕ) over Australia and Indonesia with the highest values in Australia for 31 December 2017.

https://doi.org/10.5194/acp-2019-793
Preprint. Discussion started: 21 October 2019

Atmospheric Chemistry and Physics Discussions

The differences between the northernmost city (Darwin) and the southernmost city (Melbourne) are quite large in terms of UV exposure because of differences in SZA, ozone amount, and cloud cover leading to a larger number of days per year with high UVI, a few weeks for Melbourne and three months for Darwin. This is reflected in the non-melanoma skin cancer statistics published by Australian Institute of Health and Welfare (2016) for the different regions with the Northern Territories (containing Darwin) having double the rate per 100,000 people compared to Victoria containing Melbourne (Pollack et al., 2014).

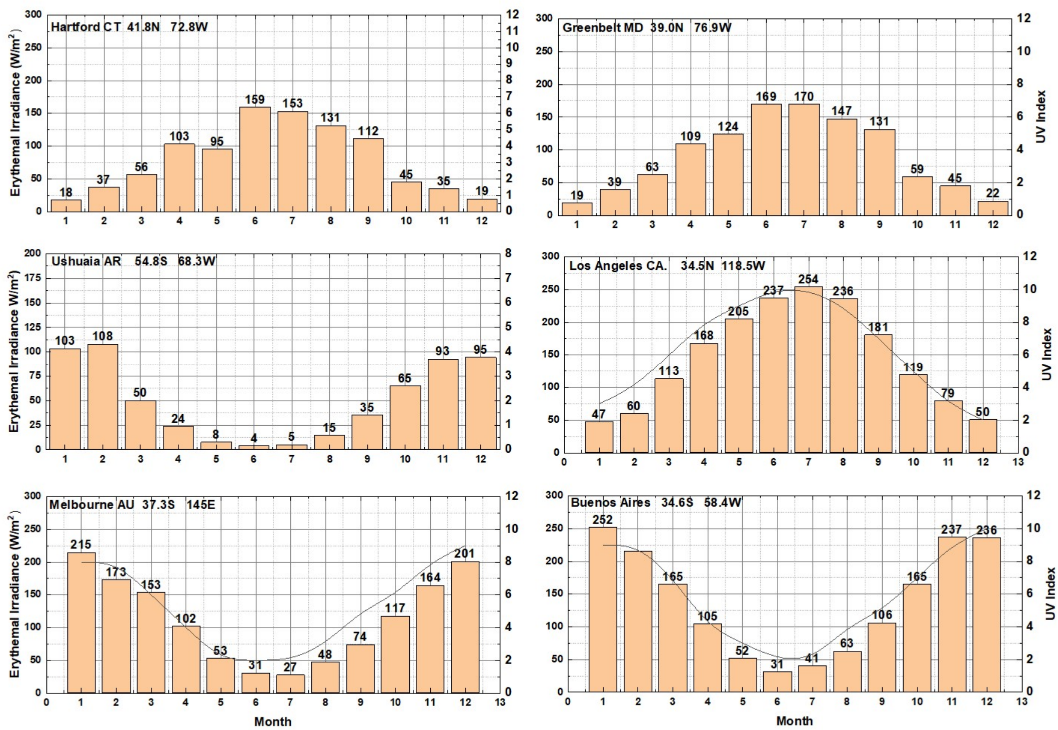

Fig. 7 Monthly average variation in E(ζ,ϕ,z,t) for six sites in both the Northern and southern Hemispheres. Solid lines are from data summarized in a World Health Organization study.

https://www.who.int/uv/intersunprogramme/activities/uv_index/en/index3.html. The small numbers are the height on the histogram bars (W/m^2).

The values of E(ζ,ϕ,z,t) over Antarctica, Fig. 6, are likely not accurate because the reflectivity of the scene is approximately treated as if there were a thin cloud over a bright surface. The calculated transmission function T(ζ,ϕ,t) has a minimum of 0.89 resulting in a difference in E(ζ,ϕ,z,t) between setting T = 1 and using the Antarctic Peninsula calculated T(ζ=-

https://doi.org/10.5194/acp-2019-793
Preprint. Discussion started: 21 October 2019

70, ϕ=-64) of less than 10%. The annual cycle ranges from 0 in winter (May to August) to a variable maximum in December depending on the year. For example, 125 mW/m^2 in 2013 and 175 mW/m^2 in2016. The year to year variation in the maximum E(ζ,ϕ,z,t) is driven the variable ozone amount. The largest amount at ζ=-70^O, ϕ=-64^O occurred in 2013 and the smallest amount was in 2016 as measured by OMI.

The monthly averages in E(ζ,ϕ,z,t) shown in Fig. 7 have the expected strong variation with SZA and with latitude in both the Northern and Southern Hemispheres. Of the sites shown, the smallest values are in Ushuaia, Argentina with a peak average value in February of 108 W/m^2 (UVI = 4) and a minimum in June of 4 W/m^2. However, there are days when both ozone values are below 200 DU and the SZA is near its minimum (about 32^O) giving rise to UVI values of 8 (Fig. 5). This contrasts with the Los Angeles California site in Fig. 7 where the monthly average maximum is 254 W/m^2 (UVI = 10) and the average over 14 years of the daily maximum is 11 (see Table A4). Figure 7 shows a comparison of monthly average E(ζ,ϕ,z,t) for 3 sites with a World Health Organization compilation of E(ζ,ϕ,z,t) for the 21st of each month (solid line).

3 Global View of E(ζ,ϕ,t_O) distributions from DSCOVR EPIC

EPIC onboard the DSCOVR spacecraft views the sunlit disk of the Earth from a small orbit about the Earth-Sun gravitational balance point (Lagrange-1 or L_1) 1.5 million kilometers from the Earth. EPIC has 10 narrow band filters ranging from the UV at 310 nm to the near infrared, 870 nm that enable measurements of TCO_3 and LER with 18 km nadir resolution using a 2048 x2048 pixel charge coupled detector. EPIC takes multiple (12 to 22) sets of 10 wavelength images per day as the Earth rotates on its axis. The instrumental details and calibration coefficients for EPIC are given in Herman et al. (2018) as well as some examples of UV estimates.

EPIC measured UV irradiances are derived from measured TCO_3 and 388 nm LER for about 3 million grid points as shown in for 22 June 2017 at 06:13 GMT (Fig. 8). These quantities along with terrain height maps are converted into E(ζ,ϕ,z,t_O) for each grid point at the specified GMT time t_O using the algorithm given in the appendix. R = LER is converted into transmission T using T = (1 – R)/(1 – R_G), where R_G is the surface reflectivity (Herman and Celarier, 1997), on average R_G is approximately 0.05, for most scenes without snow or ice. The simple expression for T gives approximately the same results as a more elaborate analysis of clouds and aerosols averaged over large scenes as seen from EPIC (Krotkov et al., 2001). The LER map in Fig. 8 can be compared to the color image of the Earth obtained by EPIC, where the high values of LER correspond to the bright clouds shown in the color image. Ozone absorption mostly affects the short wavelength portion of the erythemal spectrum (300 – 320 nm), with only small absorption from 340 – 400 nm. The effects of Rayleigh scattering are also included. The results of combining TCO_3, LER and Rayleigh scattering to estimate erythemal irradiance are shown in Fig. 9 (upper left) for 22 June 2017 with t_O = 06:13 GMT.

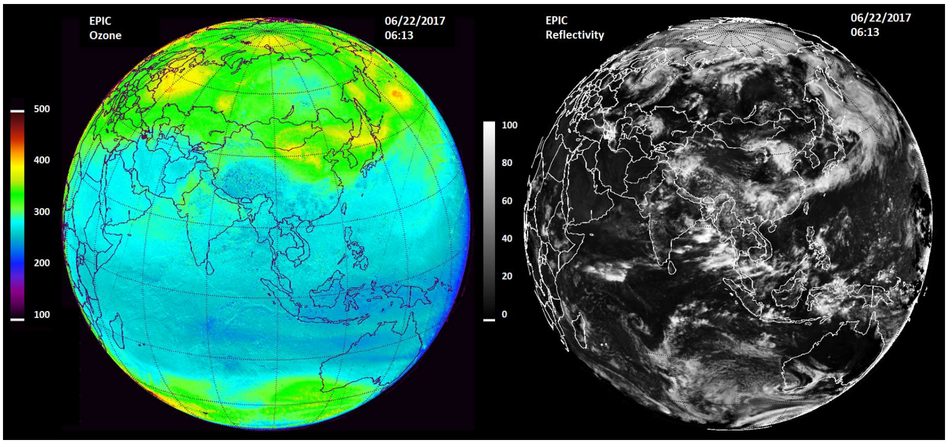

Fig. 8 EPIC derived TCO_3 (upper left in DU: 100 to 500 DU) and reflectivity (LER upper right in percent or RU: 0 to 100) for 22 June 2017 at t_O = 06:13 GMT. Lower left: color image of the Earth showing clouds and land areas. The brighter clouds are optically thick and correspond to the higher values of the LER.

The data from EPIC are synoptic (same GMT) so that the ozone, reflectivity, and erythemal results are from sunrise (west or left) to sunset (right or east) with decreasing values for SZA near sunrise and sunset. A similar erythemal darkening effect from increased SZA occurs for north and south higher latitudes. In these images, local solar noon is near the center, but offset by EPIC's viewing angle that is 4^O to 15^O away from the Earth-sun line. In the case shown, the six-month orbit is offset about 10^O to the west. Three months earlier in March and three months later in September, the orbit is offset to the east.

Erythemal maps in subsequent figures are organized by season (December and June solstices, and March and September equinoxes). The maximum values of $E(\zeta,\phi,t_O)$ follow the

https://doi.org/10.5194/acp-2019-793
Preprint. Discussion started: 21 October 2019

minimum SZA modified by cloud amount. Since the sub-solar point moves with the annual change in the Earth's declination angle (between ±23.3^{O}), the maximum UVI usually occurs at local solar noon (LST) with the smallest SZA. An exception is when the effect of increased altitude is larger than the SZA effect. An example of this is shown in Fig. 10 for the Himalayan Mountains, which contain Mt Everest. The maximum UVI for Mt Everest in Fig. 8 is 18 even though it is at about 10:30 LST (SZA = 7^{O})

3.1 Northern Hemisphere Summer Solstice (June)

For the June solstice view (Fig.9), the EPIC view includes the entire Arctic region and areas to about 55^{O}S. The center line of the image is close local solar noon. The view is with north up and from sunrise (west or left) to sunset (east or right). The effect of the orbital distance of 4^{O} to 15^{O} from the Earth-Sun line can be seen in the asymmetry of the sunrise and sunset regions implying that that the six-month orbit was off to the south-west of the Earth-sun line. The images were selected to give estimates of erythemal irradiance over Asia, Africa, and the Americas as a function of latitude, altitude, and longitude (time of the day) for a specific Greenwich Mean Time (GMT) for each map.

In Fig. 9 high UVI is seen over the Himalayans Mountains (06:13 GMT) and central western China, reaching over UVI = 18 for a June day on Mt Everest (28.0^{O}N, 86.9^{O}E, 8.85 km). On the next view in Fig. 9 over central Africa (11:21 GMT) there are elevated UVI =11, and on the third image in Fig. 9 (19:00 GMT) there is an elevated UVI area over the mountainous regions of Mexico (UVI = 16). The effect of significant cloud cover at moderate SZA can be seen (blue color), where the UVI is reduced to 2 near noon (e.g., Gulf of Mexico at 19:00 GMT). There are reductions in $E(\zeta,\phi,z,t)$ from lower reflectivity clouds in the center of the Fig.9 images that are not easily seen in the UVI image with the expanded scale (0 to 20). The effect of higher reflectivity clouds in Fig. 8 are easily seen in Fig. 9 in blue color representing low amounts of $E(\zeta,\phi,z,t)$ at the ground. There are only small percent change features in the ozone distribution, so that few ozone related structures are expected in the $E(\zeta,\phi,t_O)$ images for such a coarse UVI scale.

https://doi.org/10.5194/acp-2019-793
Preprint. Discussion started: 21 October 2019

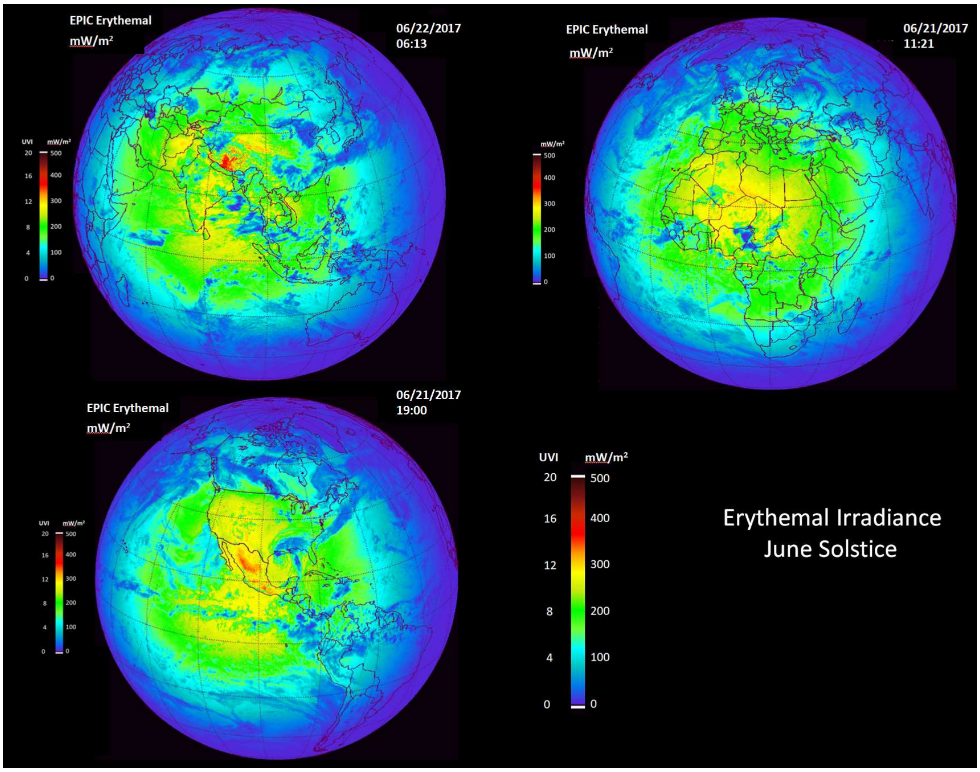

Fig.9 Erythemal irradiance E(ζ,ϕ,z,t) and UVI from sunrise to sunset for 21 June 2017 solstice. The three images are for different GMT. Upper left 22 June 2017 (06:22GMT). Upper Right 21 June 2017 (11:21 GMT) and Lower Left 21 June 2017 (19:00 GMT). The images correspond to the sub-solar points over different continents caused by the Earth's rotation (15^{O} per hour).

https://doi.org/10.5194/acp-2019-793
Preprint. Discussion started: 21 October 2019

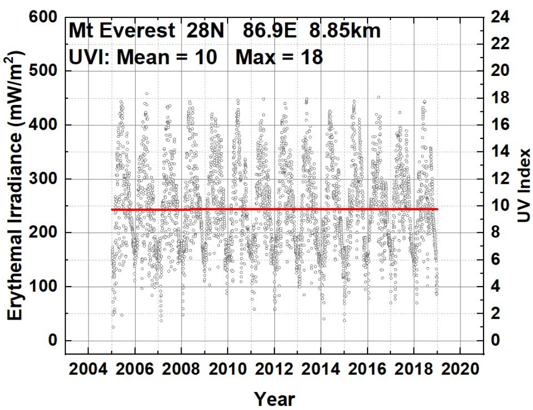

Fig. 10A E(ζ,ϕ,tO) near the summit of Mt. Everest at an altitude of 8.85 km. Mean T=0.7

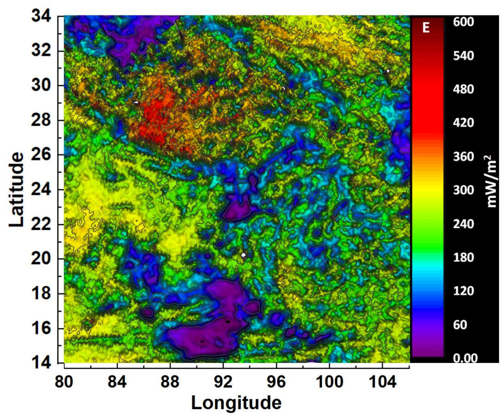

Fig. 10B Erythemal irradiance on 22 June 2017 near Mt. Everest within the Tibetan Plateau region (red color) in mW/m^2.

The E(ζ,ϕ,tO) time series for Mt Everest (Fig. 10A) at 8.85 km altitude and at 28^{O}N has a mean value of UVI = 10 and has an average annual peak occurring in June with UVI = 18 on days with little or no cloud cover. For the same conditions, except for artificially setting the altitude at sea level, the maximum UVI = 13. The sea level mean UVI value is 7. There is an average net altitude correction for maximum UVI of (18 - 13)/(13*8.8) = 4.3%/km and 5.6%/km for the mean UVI, including corrections for ozone amount and latitude (Appendix Eqn. A7).

Figure 10B shows the distribution of E(ζ,ϕ,tO) around Mt Everest (approximately 2^{O} x 2^{O}) for 22 June 2017 at 06:13 GMT (Fig. 9) and the effect of heavy cloud cover (blue and purple areas). The reflectivity in Fig. 8, shows there is a mixture of light and heavy cloud cover in the region reducing the amount of UV reaching the surface. The red region in the upper left is the location of the Mt Everest peak with very high values of UVI. The yellow colors represent high UVI values of about 10 and green about 8. Winter values at the top of Everest ae quite low as shown in Fig. 10A ranging from UVI =2 to 4 depending on cloud cover.

https://doi.org/10.5194/acp-2019-793
Preprint. Discussion started: 21 October 2019

411 **3.2 E(ζ,ϕ,t_O) for September and March Equinox Conditions**

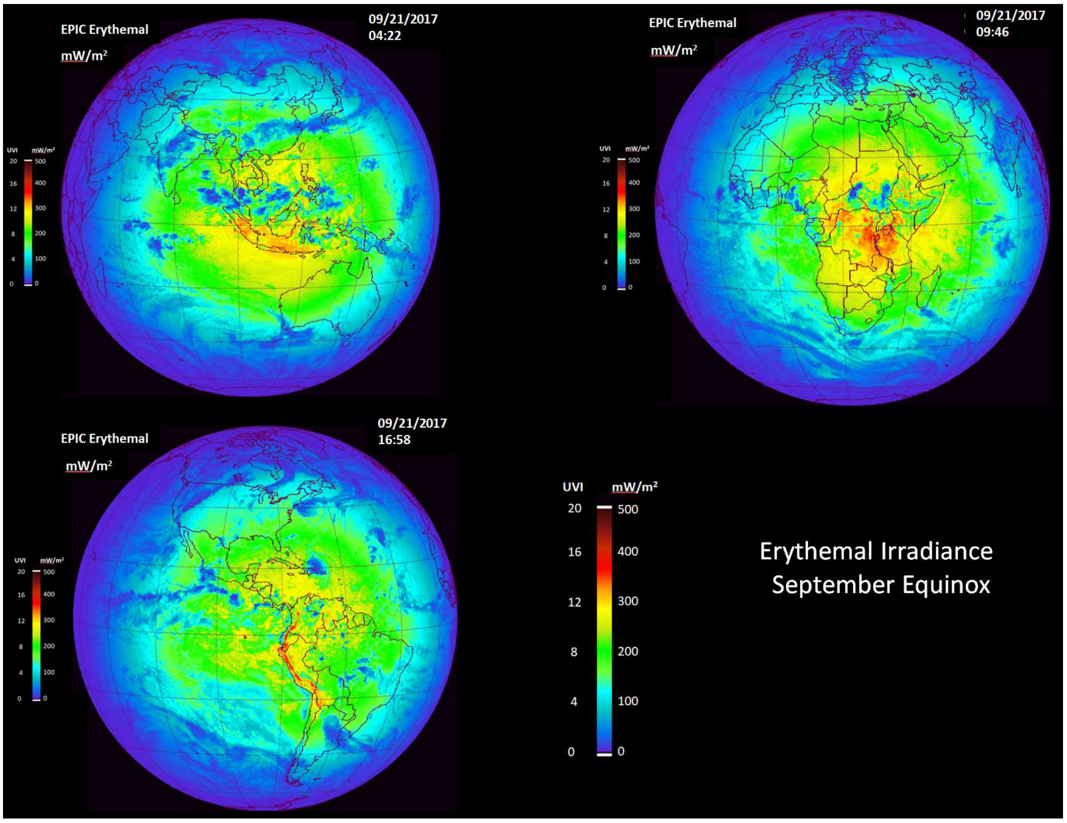

Fig. 11A E(ζ,ϕ,t_O) and UVI from sunrise to sunset for 21 September 2017 equinox. The three images are for different GMT

412

413 Near the September and March equinoxes (Figs. 11A and 11B) the sun is overhead near
414 the Equator giving high UVI = 12 in many areas with higher values (16 to 18) in the mountain
415 regions (e.g., Southern Indonesia, Peru's Andes Mountains, and some high-altitude regions in
416 Malawi and Tanzania. While the Sun-Earth geometry is nearly the same for both equinoxes,
417 there is considerable difference in seasonal cloud cover for the two equinox days. The area of
418 sub-Saharan Africa near Nigeria has particularly high UVI values caused by nearly cloud-free
419 conditions over a wide region implying a considerable heath risk for mid-day UV exposure.
420 Other high UVI values occur over smaller elevated areas. This is particularly evident in the
421 nearly cloud-free high-altitude Peruvian Andes at about 28^{O}S even though the SZA = 28^{O}.

https://doi.org/10.5194/acp-2019-793
Preprint. Discussion started: 21 October 2019

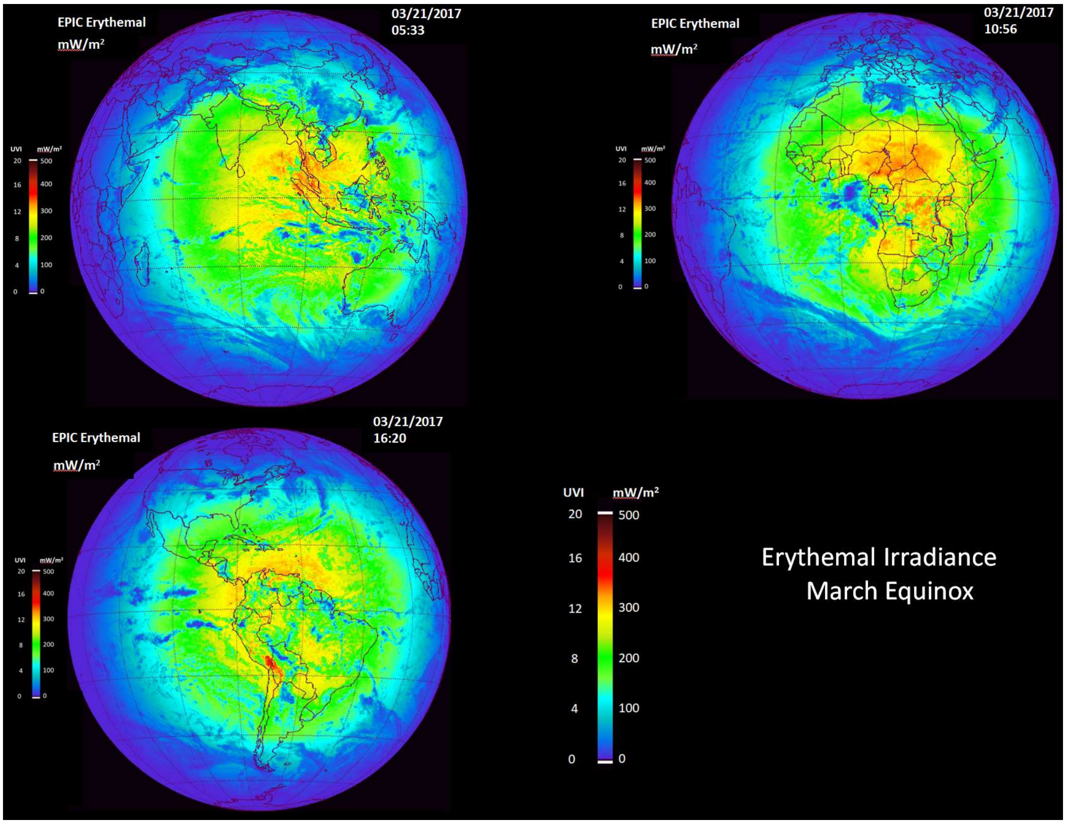

Fig. 11B E and UVI from sunrise to sunset for 21 March 2017 equinox. The three images are for different GMT (05;33, 10:56, and 16:20).

3.3 Southern Hemisphere Summer Solstice (December)

During the December solstice the sun is overhead at 23.3^{O}S (Fig. 12). The reduced SZA causes high UVI levels throughout the region between 20^{O}S and 40^{O}S especially in elevated regions such as the Chilean Andes, Western Australia and elevated regions of southeastern Africa (South Africa, Tanzania, Kenya). For the case where Western Australia is near local solar noon, the UVI levels reach about 13 to 14 between 20^{O}S to 34^{O}S, a region that includes the city of Perth with more than a million people and several smaller cities and towns. These high UVI values represent a considerable health risk for skin cancer, since the UVI stays above 12 for nearly a month. The same is true for eastern Australia (Fig. 6) during December that implies the high skin cancer risk for the entire Australian continent. The same comments apply to New Zealand, eastern South Africa and elevated areas further north (e.g., Tanzania Africa). Even

https://doi.org/10.5194/acp-2019-793
Preprint. Discussion started: 21 October 2019

Atmospheric Chemistry and Physics Discussions
Open Access

higher values occur in the Andes Mountains in Chile and Peru that include some small cities (see Fig. 4 for San Pedro de Atacama, Peru).

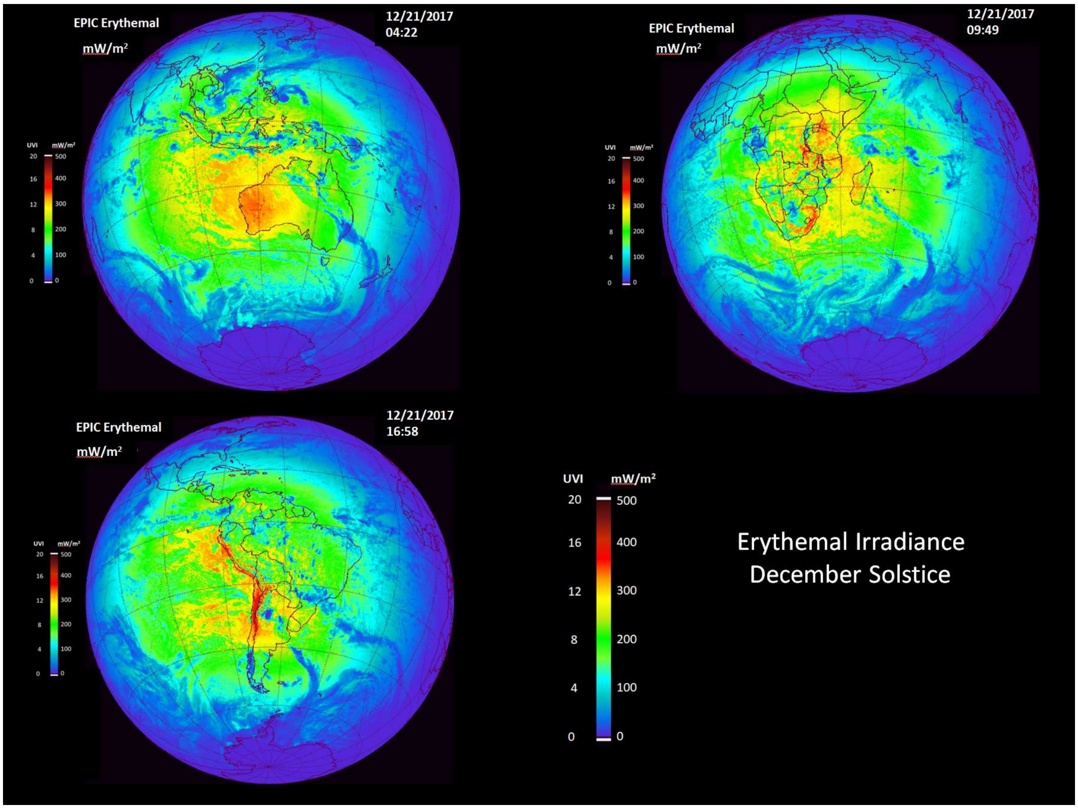

Fig. 12 $E(\zeta,\phi,t_O)$ and UVI from sunrise to sunset for 21 December 2017 solstice. The three images are for different GMT.

3.4 Erythemal Synoptic Variation (Sunrise to Sunset)

The longitudinal dependence of $E(\zeta,\phi,t_O)$ is illustrated in Fig. 13 where sunrise to sunset slices have been taken for an equatorial latitude, 0.1^ON and mid-latitude, 30.85^ON. The estimated $E(\zeta,\phi,t_O)$ includes the effect of clouds and haze (Panels C and D) included in the atmospheric transmission function $T(\zeta,\phi,t_O)$ and the effects of local terrain height. The maximum $E(\zeta,\phi,t_O)$ is to the east of the sub-satellite point because the satellite orbit about the Lagrange-1 point L_1 is displaced to the west of the Earth-Sun line on 14 April 2016. The northward displacement is caused by the Earth's declination angle of about 9.6^O. This corresponds to the minimum SZA shown in Fig. 13A Panel A of 9.5^O. Panels A, B, C, D show the effects of cloud transmission for all values of LER that are not easily seen in the global erythemal color maps (bottom panels of Fig. 13A. The presence of clouds is easily seen in the color image for 14 April at 4:21 GMT (Fig. 13B).

https://doi.org/10.5194/acp-2019-793
Preprint. Discussion started: 21 October 2019

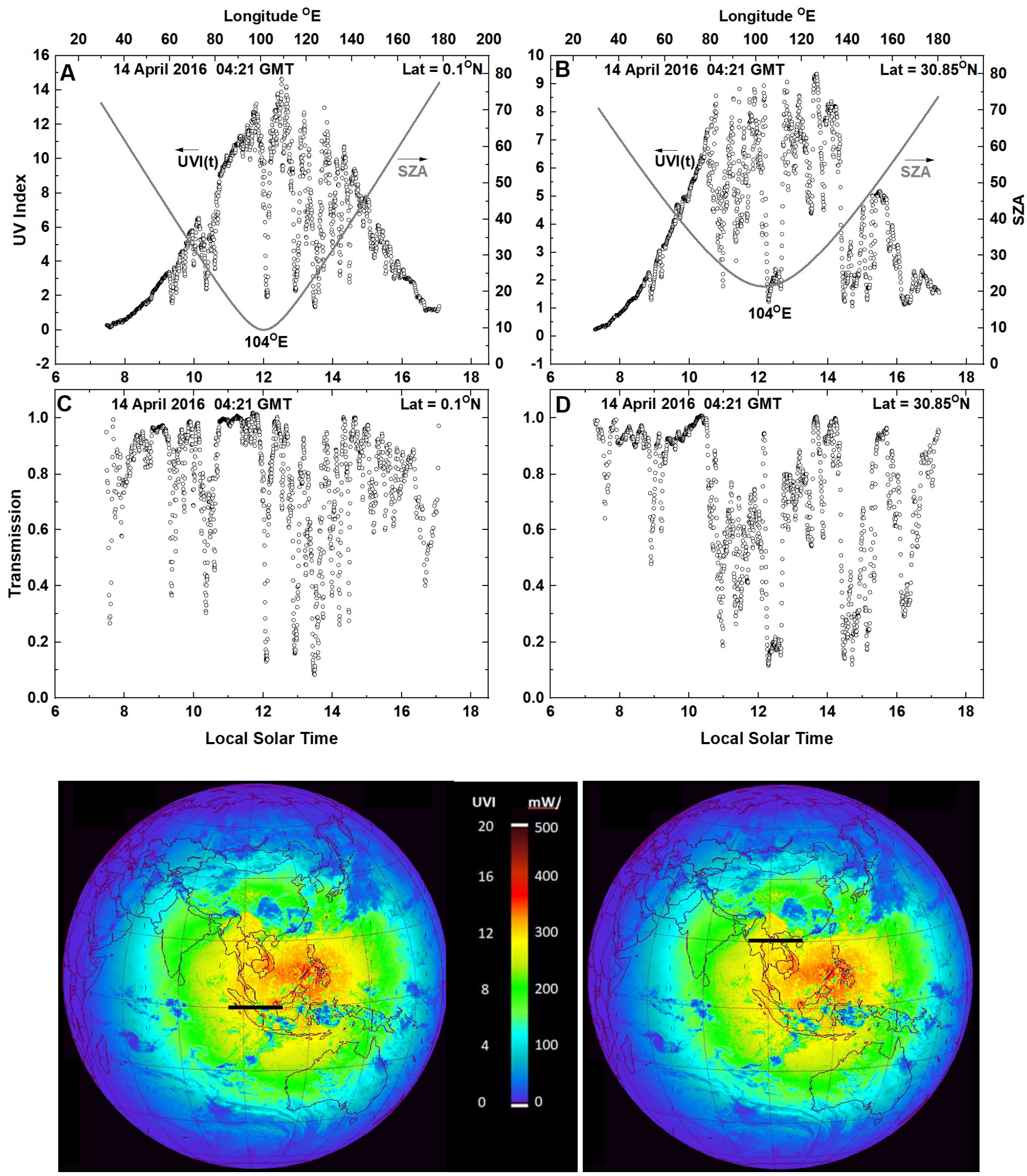

Fig. 13A Longitudinal slices of E(ζ,ϕ,t_O) (units UVI) at 0.1°N and 30.85°N latitude shown by the dark horizontal bars. The EPIC E(ζ,ϕ,t_O) images are for 14 April 2016 t_O = 04:21 GMT centered at about 10°N and 104°E. Panels A and C show longitudinal slices of E(ζ,ϕ,t_O) and T(ζ,ϕ,t_O) for ζ = 0.1°N and panels B and D for 30.85°N. The solid lines in panels A and B represent the SZA.

https://doi.org/10.5194/acp-2019-793
Preprint. Discussion started: 21 October 2019

Atmospheric Chemistry and Physics Discussions

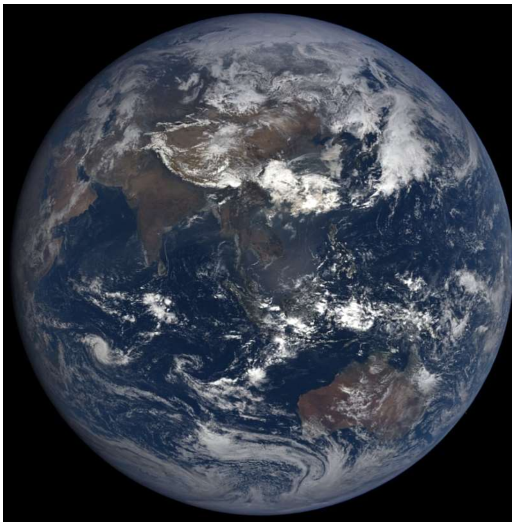

Fig 13B EPIC color image for 14 April 2016 at 04:12:16 GMT showing the distribution of cloud cover and land corresponding to Fig. 13A

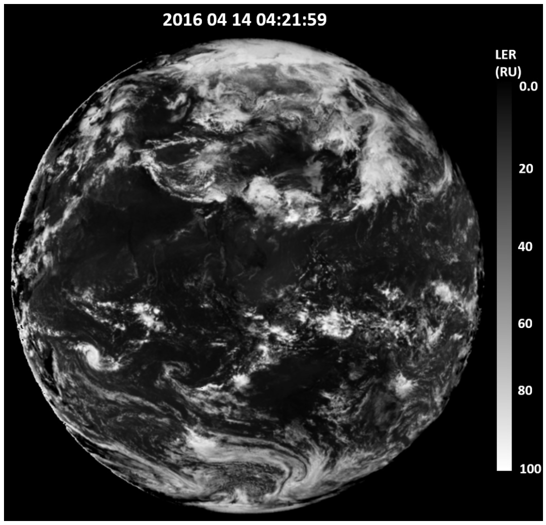

Fig 13C EPIC scene reflectivity LER for 14 April 2016 at 04:12:16 GMT

The main cause of the decrease of $E(\zeta,\phi,t_O)$ with latitude between 0.1^{O}N and 30.85^{O}N is caused by the increased SZA followed by the latitudinal increase in TCO_3. The difference is modulated (Panels A and B) by the presence of clouds and haze (Figs. 13B and 13C) and haze in $T(\zeta,\phi,t_O)$ shown in Fig. 13A Panels C and D. There are nearly clear-sky patches for the equatorial sample leading to very high UVI = 14 compared to the mid-latitude maximum of UVI = 9 because of the effect of clouds near the time of minimum SZA. The distribution of clouds is shown in the true color picture of the Earth obtained by EPIC on 14 April 2016 at 04:12:16 GMT centered on 104^{O}E. The bright white portion of cloud mages are the optically thick clouds of high reflectivity and low transmission.

3.5 Zonal average $E(\zeta,\phi,t_O)$ and 14-Year Trends

Figure 14 shows a summary of the zonal maximum (Panel A) and zonal average (Panel B) UVI values on 14 April 2016 at 04:21 GMT from Fig. 13A for longitudinal bands plots from $-75^{O} <$ Latitude $< 75^{O}$. The solid lines are a smooth Akima spline fit (Akima, 1970) to the data points. Depending on the day of the year, the location of the maximum will shift between -23.45^{O} to $+23.45^{O}$ following the position of overhead sun. The zonal average maximum (Fig. 14A) of about UVI = 14 is approximately the same for any day of the year. This includes longitudes containing high altitude sites at moderately low latitudes where the local UVI maximum can reach 18 to 20. The US Environmental Protection Agency classifies exposure at UVI=6 to 7 as high, which requires protection for extended exposure (e.g., 1 hour). For low latitudes, UVI > 6 occurs several hours around local solar noon. For equatorial latitudes at sea level, UVI > 6 occurs for about 6 hours (Fig. 13). The zonal average values (Fig.14B) are considerably smaller, since they are more affected by clouds than the mostly clear-sky maxima in Fig. 14A.

https://doi.org/10.5194/acp-2019-793
Preprint. Discussion started: 21 October 2019

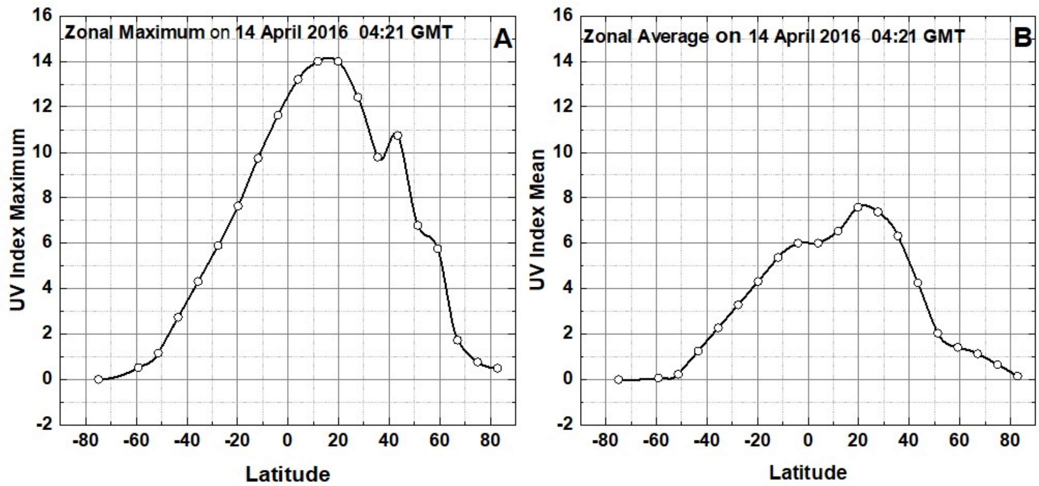

Fig. 14 Zonal Maximum UVI (Panel A), Zonal Average (Panel B) on 14 April 2016 at 04:21 GMT from EPIC including the effect of clouds and haze, as a function of latitude. Both the data points and an Akima spline fit are shown.

Of interest are similar analyses of the 105 land sites as listed in the Appendix Table A4 and summarized in Figs. 15 and 16. The results over 14 years show much higher levels of UVI than for the single day zonal average shown in Fig. 14, especially for the four indicated high-altitude sites. The maximum summer values at all latitudes between 60^{O}S and 60^{O}N exceed UVI = 6, which is considered high enough to cause sunburn for unprotected skin (Sánchez-Pérez et al., 2019) in 20 to 50 minutes depending on skin type. Higher values of UVI can produce sunburn in much shorter times. For example, for UVI = 10, sunburn can be produced in as little as 15 to 30 minutes exposure of unprotected skin.

The highest UVI values in Table A4 are associated with 4 sites at high altitudes. Two of these are populated cities, San Pedro de Atacama (Population = 11,000), Chile and La Paz Bolivia (Population = 790,000). These two sites have very high UVI because of their altitude, low latitude, and relative lack of clouds on some days. Over the 14 years of this study, the UVI at San Pedro de Atacama has remained approximately constant while at La Paz, Bolivia the UVI has decreased at a rate of 4.6 ± 0.05% per decade caused by an increase in ozone amount (1.4 ± 0.1 % per decade) and a decrease in atmospheric transmission (-3.2 ± 0.5 % per decade).

https://doi.org/10.5194/acp-2019-793
Preprint. Discussion started: 21 October 2019

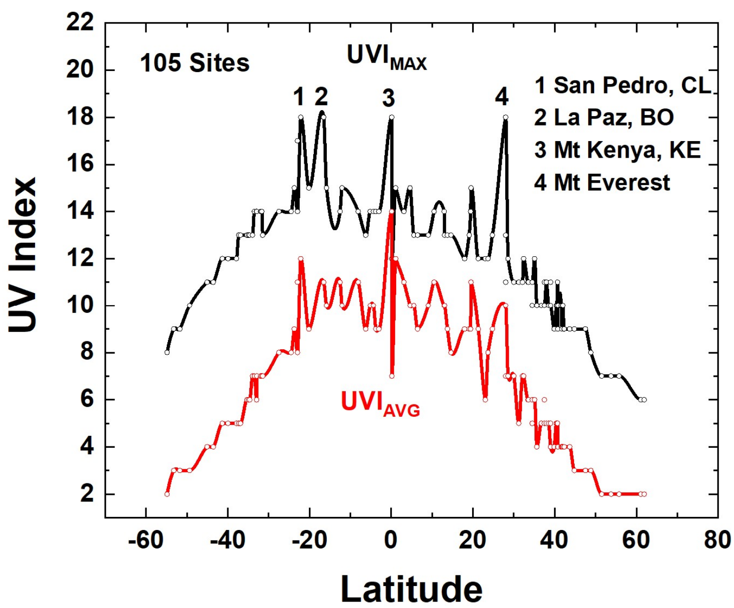

Fig. 15. Fourteen-year UVI Average and UVI Maximum from Table A4 for 105 sites. Solid curves are Akima spline fits to the individual site data points. There are 4 high altitude sites listed, San Pedro, Chile (2.45 km), La Paz, Bolivia (3.78 km), Mt Kenya, Kenya (5.2 km), and Mt Everest, Nepal and China (8.85 km).

Table A4 also presents the 14-year linear LS trends of changes in erythemal irradiance, Atmospheric Transmission, and column ozone amount (%/Yr) and the 1-σ error estimate for those trends. The results are summarized in Figs.16 for the 105 selected land sites. There is significant variation in atmospheric transmission, ± 0.2%/Yr, (mostly cloud reflectivity) for an extended latitude range, 55^{O}S – 35^{O}N. However, on average there is no systematic change as indicated by the local least squares fit (red line Lowess(0.5)). For latitudes greater than 40^{O}N atmospheric transmission has increased (cloud reflectivity decreased) for the period 2005 to 2018 implying that solar insolation has also increased for all UV (305 – 400 nm), visible wavelengths (400 – 700 nm), and near infrared wavelengths (700 – 2000 nm). For the UV portion of the spectrum represented by the erythemal irradiance action spectrum, the change is affected by changes in TCO_3. The TCO_3 changes (Fig. 16C) result in an average decrease in irradiance for latitudes between 55^{O}S and 35^{O}N and a smaller %/Yr increase for higher latitudes than would be expected based on non-absorbing atmospheric transmission changes. The ozone changes obtained from OMI observations include the effects of the 11.3-year solar cycle, the quasi-biennial oscillation QBO, and the El Nino Southern Oscillation ENSO effects, and, as such, are not the standard ozone trend amounts (Weber et al., 2017).

https://doi.org/10.5194/acp-2019-793
Preprint. Discussion started: 21 October 2019

Atmospheric Chemistry and Physics
Open Access
Discussions

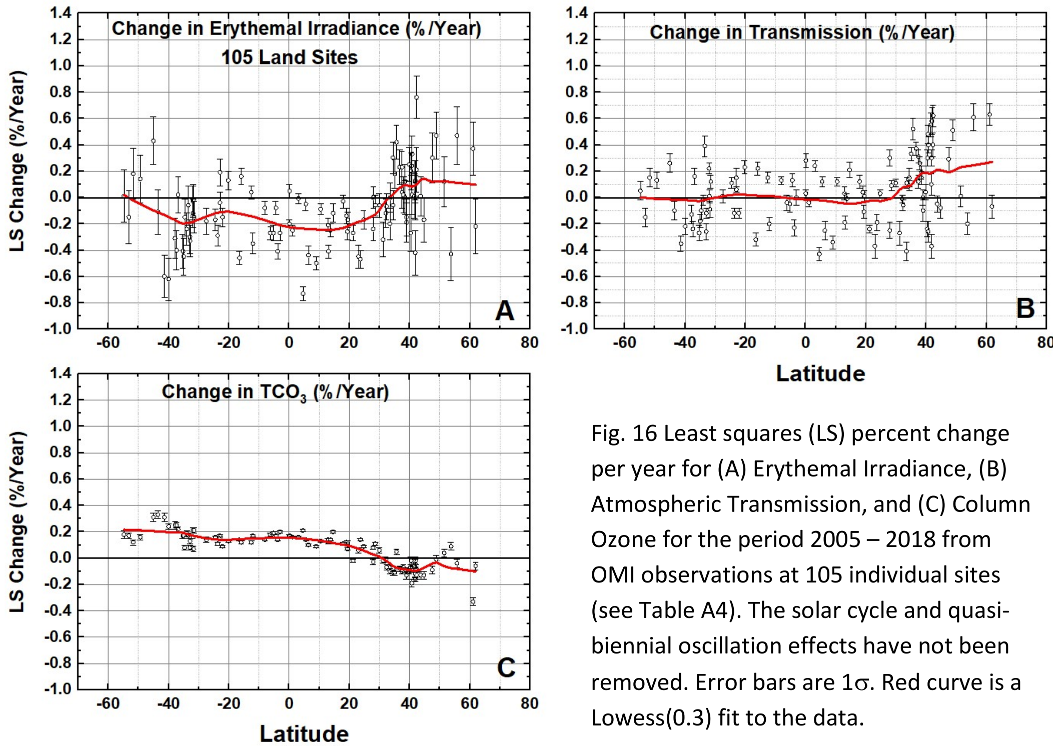

Fig. 16 Least squares (LS) percent change per year for (A) Erythemal Irradiance, (B) Atmospheric Transmission, and (C) Column Ozone for the period 2005 – 2018 from OMI observations at 105 individual sites (see Table A4). The solar cycle and quasi-biennial oscillation effects have not been removed. Error bars are 1σ. Red curve is a Lowess(0.3) fit to the data.

Similar changes can be estimated over the Atlantic and Pacific oceans for an extended latitude range from 60^{O}S to 60^{O}N without intersecting land at 30^{O}W (Atlantic) and 179^{O}W (Pacific) in steps of 5^{O} latitude (Fig. 17). The percent change per year over the Atlantic Ocean at 30^{O}W at high northern latitudes is the opposite of those occurring over land with a decrease in transmission (increase in reflectivity) implying a decrease in solar insolation. A similar analysis over the Pacific Ocean at 179^{O}W shows a change that shows an increase in transmission at high northern latitudes of the same magnitude as occurs over land implying increased solar insolation over a wide wavelength range (380 – 2000 nm). In the UV range the erythemal irradiance changes follows the changes in transmission offset by the smaller changes in column ozone amount.

The band of equatorial cloud reflectivity has decreased (transmission increased) for both the Atlantic and Pacific Oceans at 0^{O} and at 5^{O}N. For the Pacific at 179^{O}W, the estimated changes correspond to the El Nino Southern Oscillation ENSO region suggesting a decrease in cloud reflectivity. On either side at 5ON and 10OS there is a decrease in transmission of about 2% per decade over the Atlantic and about 4 to 5%/decade over the Pacific ENSO longitude.

https://doi.org/10.5194/acp-2019-793
Preprint. Discussion started: 21 October 2019

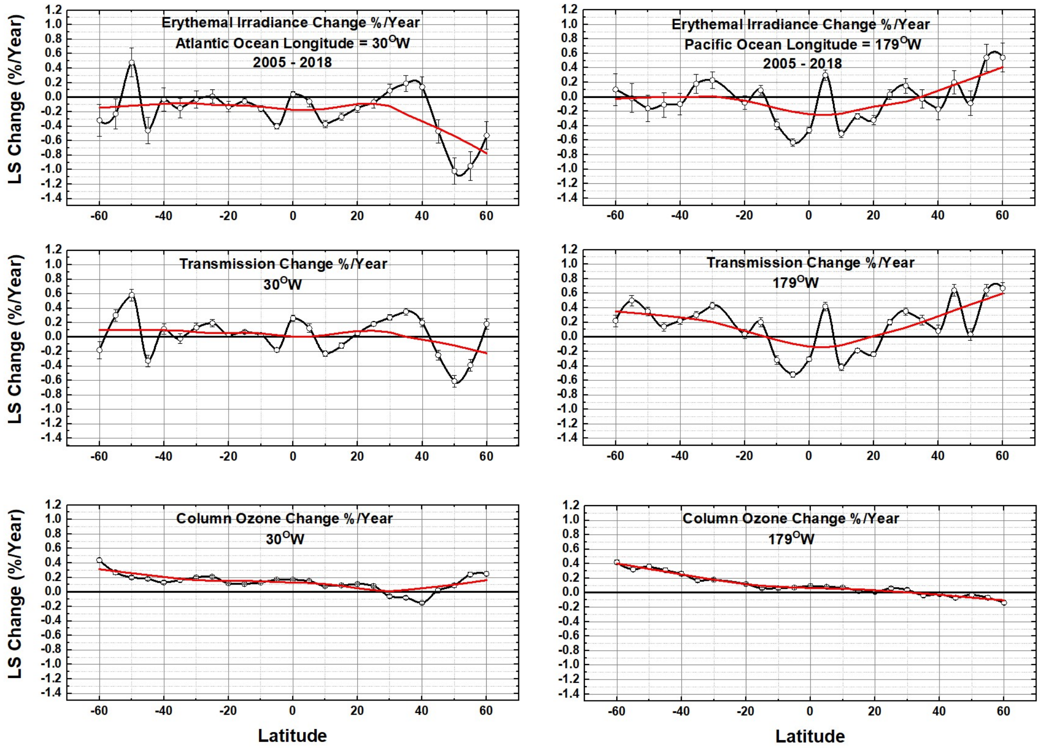

Fig. 17: Similar to Fig. 16 but over the Atlantic (Longitude 32°W) and the Pacific (179°W) Oceans with one data point every 10° of latitude.

516

517 Figure 18 shows the changes that have occurred over the major landmasses as a function of latitude over specified longitudes, A. Europe Africa 20°E, B. North America 90°W, B. South America 60°W, and D. Russia-China-India 120°W. The results are quite variable with North America showing the increase in the rate of transmission T increase at high latitudes offset in E by a small increase in TCO_3. Europe-Africa also shows the increase in the rate of T increase that is bigger in effect than a small decrease in TCO_3. South America shows little change, but the northern part of the graph is over the Atlantic Ocean at 60°W and shows rates that are different from North America at 90°W.

524

https://doi.org/10.5194/acp-2019-793
Preprint. Discussion started: 21 October 2019

Atmospheric Chemistry and Physics Discussions

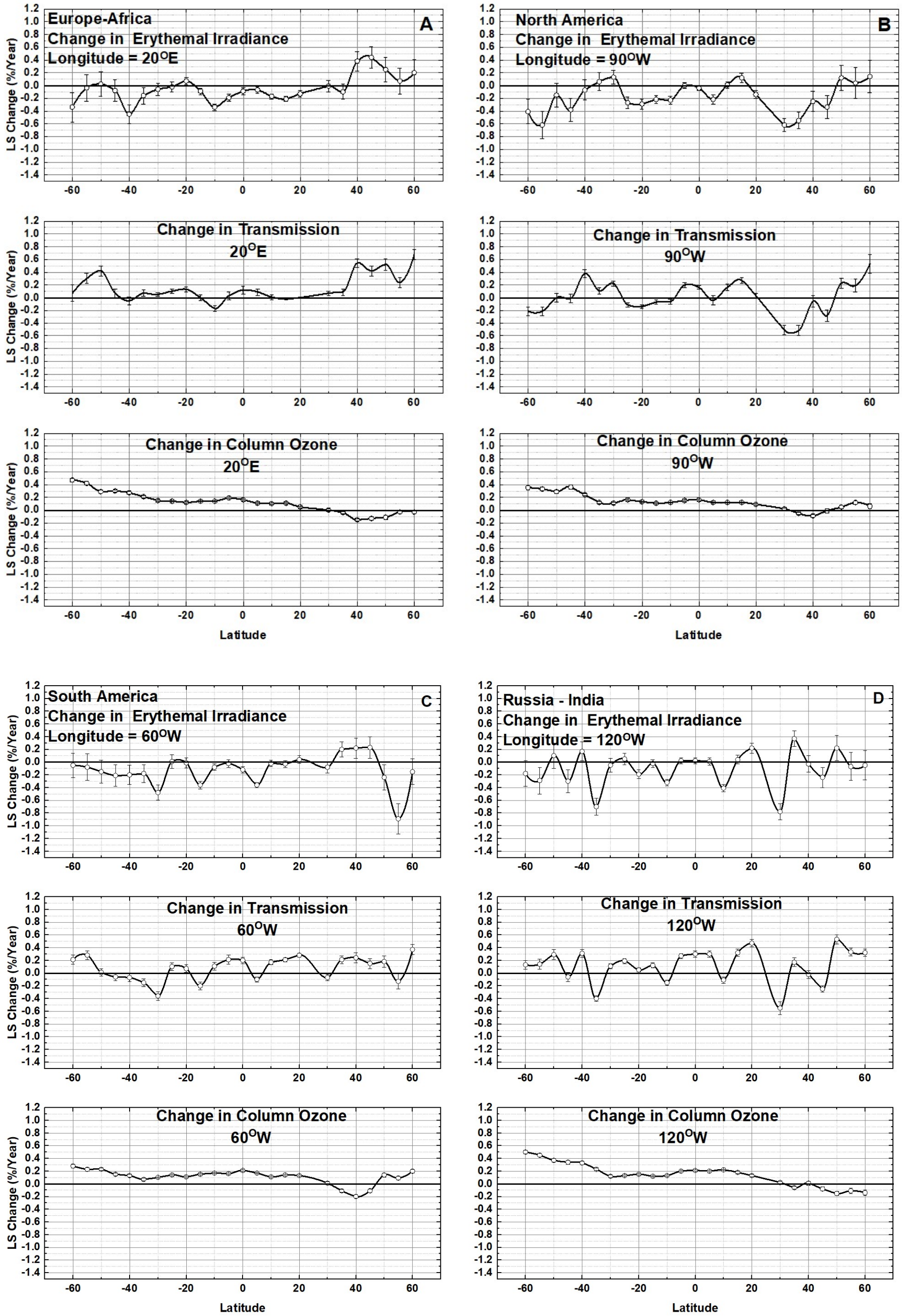

Fig. 18 Similar to Fig. 17 but for land areas as indicated for longitudes 20°E, 90°W, 60°E, 120°W

https://doi.org/10.5194/acp-2019-793
Preprint. Discussion started: 21 October 2019

Atmospheric Chemistry and Physics
Open Access
EGU
Discussions

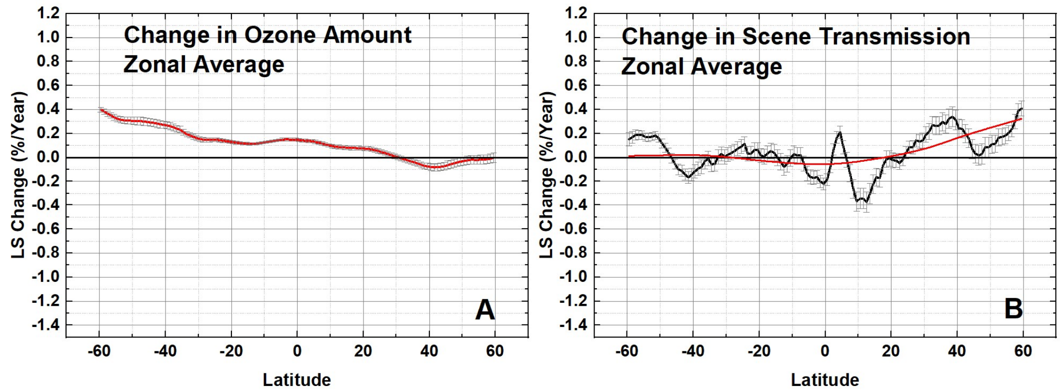

Fig. 19 Zonal average of change in OMI column ozone amount and in atmospheric transmission (%/Yr). The red line in Fig. 19B is a Lowess(0.5) fit showing the general trend as a function of latitude.

Figure 19A shows the zonal average percent change per year computed every 2.5^{O} for $TCO_3(\zeta)$ and for the atmospheric transmission function $T(\zeta)$. TCO_3 is showing increases for Southern latitudes and for latitudes up to 20^{O}N. As mentioned earlier, the ozone trend includes the effects of the solar cycle, QBO, and ENSO effects, which is appropriate for this study of erythemal irradiance and its changes. The NASA OMI project suggests that there may be an OMI drift of +0.1% per year (private communication) relative to a reference TCO_3 data set derived from the overlap (2012 – 2018) with NOAA 19 SBUV/2 (National Oceanographic Atmospheric Administration Solar Backscatter Ultra Violet - 2) instrument. The effect of this systematic drift would be to shift the curve in Fig. 19A downward by 0.1%/Year or be considered as an uncertainty that is greater than the small statistical uncertainties. Figure 19B shows the zonal average percent change per year for atmospheric transmission $T(\zeta)$ caused by the presence of aerosols and clouds where $T(\zeta,t)$ has been normalized to the assumed invariant Antarctic high plateau ice reflectivity. The results indicate that there is on average increased solar insolation for high northern latitudes. The decreased cloud cover suggests a positive feedback mechanism for global warming.

4 Summary

Measured total column ozone TCO_3 and Lambert Equivalent Reflectivity LER (converted to atmospheric transmission) data $T(\zeta,\phi,z,t)$ from AURA-OMI have been combined along with terrain height data to estimate noon time series for erythemal irradiance $E(\zeta,\phi,z,t)$ in mW/m^2 (or UVI = E/25) reaching the Earth's surface at globally distributed specified locations using Eqns. A1 to A9. This paper summarizes the results from 182 land plus ocean locations, some having dangerously high values of UVI caused either by the presence of low SZA and ozone values or high altitudes under almost clear-sky conditions. For some sites, there has been no long-term LS linear change (2005 – 2018) in UVI at the two-standard deviation level 2σ. However, nearly half the sites have shown 2σ changes in UVI caused by changes in atmospheric transmission (clouds plus aerosols) and an offset from zero caused by changes in ozone amount. Fourteen-year atmospheric transmission trends are calculated showing little change in average T (mostly cloud reflectivity) from 55°S to 35°N, but with significant increase in T from 40°N to 60°N causing increased solar insolation from the UV to NIR wavelengths at these latitudes suggesting positive feedback from global warming. TCO_3 also shows significant latitudinal change with an increase between 55°S to 35°N and a decrease from 40°N to 60°N that only affects UV wavelengths (300 – 340 nm). The maximum UVI is shown for each selected site with, as expected, low latitudes and elevated sites showing the highest UVI values (14 to 18) compared to typical NH mid-latitude sites at low altitude having a maximum UVI = 8 to 10. The OMI based results show agreement with monthly average values data summarized in a World Health Organization study and with measurements of UVI made in Argentina (Cede et al., 2002; 2004). Global synoptic maps of UVI from sunrise to sunset are shown from DSCOVR/EPIC data for specific days corresponding the solstices and equinoxes. These show the high UVI values occurring at local solar noon over wide areas and especially at high altitudes and the decrease with SZA caused by latitude and solar time. Figure 14 shows a zonal average for 14 April 2016 from EPIC data showing latitudes of very high UVI that track the seasonal solar declination angle corresponding to hemispheric summer. Similarly, Fig.15 shows the zonal average of the 105 land sites in Table A4 that includes 4 very high-altitude sites with UVI = 18. The EPIC and OMI observations show that there are are the wide areas between 20° and 30°S latitude during the summer solstice in Australia (Fig.12) showing near noon values with UVI = 14, values that are dangerous for production of skin cancer and eye cataracts and correlate with Australian National Institute of Health and Welfare cancer incidence health statistics (2016). Similar values of high UVI occur for the latitude range ±30° that includes parts of Africa and Asia. Two equatorial region high altitude cities, San Pedro, Chile (2.45 km), La Paz, Bolivia (3.78 km), with frequently clear sky conditions have very high UVI_{MAX} = 17 and 18 and UVI_{AVG} = 11 in contrast to Quito, Ecuador (2.85 km) that has substantial cloud cover UVI_{MAX} = 11 and UVI_{AVG} = 7. Cities located at sea level in the equatorial zone also can have high vales of UVI_{MAX} = 15 (e.g., Lima, Peru).

https://doi.org/10.5194/acp-2019-793
Preprint. Discussion started: 21 October 2019

Atmospheric Chemistry and Physics Discussions

Appendix

Some of the contents of this appendix are reproduced for convenience from Herman et al. (2018) and Herman (2010). Fitting error estimates from solutions of the radiative transfer equations are given in Herman (2010). The notation used in Herman (2010) and Herman et al., 2018 is retained with SZA = Solar Zenith Angle, θ = SZA, Ω = total column ozone amount in DU TCO_3, λ = wavelength in nm, and C_T = fractional cloud + haze transmission T. An improved numerical fit for the altitude dependence is provided for Eqn. A7 and for the coefficients in Eqn. A8.

Erythemal irradiance $E_0(\theta, \Omega, C_T)$ at the Earth's sea level (W/m^2) is defined in terms of a wavelength dependent weighted integral over a specified weighting function $A(\lambda)$ times the incident solar irradiance $I(\lambda,\theta,\Omega,C_T)$ (W/m^2) (Eq. A1). The erythemal weighting function $Log_{10}(A_{ERY}(\lambda))$ is given by the standard erythemal fitting function shown in Eq. A2 (McKinley and Diffey, 1987). Tables of radiative transfer solutions for D_E = 1 AU are generated for a range of SZA ($0 < \theta < 90^O$), for ozone amounts $100 < \Omega < 600$ DU, and terrain heights $0 < Z < 5$ km using an approximation to the solutions from the TUV DISORT radiative transfer model as described in Herman (2010) for erythemal and other action spectra (e.g., plant growth PLA, vitamin-D production VIT, cataracts CAT, etc.). The irradiance weighted by the erythemal action spectrum is given by

$$E_0(\theta,\Omega,C_T) = \int_{250}^{400} I(\lambda,\theta,\Omega,C_T)A(\lambda)d\lambda \qquad \text{(A1)}$$

$250 < \lambda < 298$ nm	$Log_{10}(A_{ERY}) = 0$	(A2)
$298 < \lambda < 328$ nm	$Log_{10}(A_{ERY}) = 0.094\ (298 - \lambda)$	
$328 < \lambda < 400$ nm	$Log_{10}(A_{ERY}) = 0.015\ (139 - \lambda)$	

Equation A1 can be closely approximated by the power law form (Eq. A3), where $U(\theta)$ and $R(\theta)$ are fitting coefficients ($R(\theta)$) is an improved Radiation Amplification Factor that is independent of Ω) to the radiative transfer solutions in the form of rational fractions (Herman, 2010). Rational fractions were chosen because they tend to behave better at the ends of the fitting range than polynomials with comparable fitting accuracy.

$$E_0(\theta,\Omega,C_T) = U(\theta)\ (\Omega/200)^{-R(\theta)} C_T \qquad \text{(A3)}$$

$$U(\theta) \text{ or } R(\theta) = (a+c\theta^2+ex^4)/(1+b\theta^2+d\theta^4+f\theta^6) \quad r^2 > 0.9999 \qquad \text{(A4)}$$

$$C_T = (1-LER)/(1-R_G) \text{ where } R_G \text{ is the reflectivity of the surface} \qquad \text{(A5)}$$

$$E(\theta,\Omega,z) = E_0(\theta,\Omega)\ H(\theta,\Omega,z) / D_E^2 \qquad \text{(A6)}$$

https://doi.org/10.5194/acp-2019-793
Preprint. Discussion started: 21 October 2019

Atmospheric Chemistry and Physics Discussions
Open Access
EGU

Numerically, $H(\theta,\Omega,z)$ is calculated by forming the ratio $R_E = E(\theta,\Omega,z)/E_0(\theta,\Omega,0)$

Where most of the θ and Ω dependence is contained in E_O

$$H(\theta,\Omega,Z) = [(-3.8443E\text{-}3\ Z_{km}+3.1127E\text{-}4)\ \Omega/200 + 0.054111\ Z_{km}+1]\ G(\theta) \qquad (A7)$$

$$G(\theta) = g+h\theta+i\theta^2+j\theta^3+k\theta^4 \qquad (A8)$$

The coefficients a, b, c, d, e, f, g, h, j, and k are in Tables A1 and A2

When Eq. A6 is applied to the ozone and LER data, the global $E(\theta,\Omega,z)$ at the Earths' surface can be obtained after correction for the Earth-Sun distance D_E, where D_E in AU can be approximated by (Eq. A9),

$$D_E = 1 - 0.01672 \cos(2\pi\ (\text{day\_of\_year} - 4)/365.25) \qquad (A9)$$

Table A1 Coefficients $R(\theta)$ and coefficient $U(\theta)$ for $0 < \theta < 80^O$ Eq. A4 and $100 < \Omega < 600$ DU for $E(\Omega,\theta) = U(\theta)\ (\Omega/200)^{-R(\theta)}$ (1.0E10 = $1.0\text{x}10^{10}$)

$U(\theta)$ or $R(\theta) = (a+c\theta^2+e\theta^4)/(1+b\theta^2+d\theta^4+f\theta^6)$ $r^2 > 0.9999$ (see Fig. A1)

Action Spectra	$U(\theta)$ (watts/m^2)	$R(\theta)$
CIE Erythemal U_{ERY} & R_{ERY}	a= 0.4703918683355716 b= 0.0001485533527344676 c= -0.0001188976502179551 d= 1.915618238117361E-08 e= 7.693069873238405E-09 f= 1.633190561844982E-12	a= 1.203020609002682 b= -0.0001035585455444773 c= -0.00013250509260352 d= 4.953161533805639E-09 e= 1.897253186594168E-09 f= 0.0

Table A2 Solar Zenith angle function $G(\theta)$ used in Eq. A8

$$G(\theta) = g+h\theta+i\theta^2+j\theta^3+k\theta^4$$

g= 9.999596516311959E-01	j= 1.752907417831904E-07
h= 2.384464204972423E-05	k= -2.482705952292921E-09
i= 3.078822311353050E-06	

Since $R_E(\theta,\Omega)$ has only weak θ and Ω dependence an approximation can be obtained by forming the mean of R_E over θ and Ω. Then a linear approximation is

$$H(z) = 1 + 0.047\ Z_{km} \qquad (A10)$$

Equation A10 is similar to Eqn. A7 with $G(\theta)$=1 and Ω = 300 DU

https://doi.org/10.5194/acp-2019-793
Preprint. Discussion started: 21 October 2019

$$H(300, Z) = 1 + 0.052\, Z_{km} \quad (A12)$$

Table A4 Summarizes the erythemal irradiance E(θ,Ω,z) and its rate of change for specific locations (Latitude, Longitude, and Altitude) based on the algorithm from Eqns. A1 - A9. C_T includes the effect of both cloud and aerosol transmission to the surface (for non-absorbing aerosols). Absorbing aerosols (ephemeral smoke and dust aerosols) are not included. Also included are the rates of change for ozone over the 14-year period.

Sites that have trends statistically significant at the two-standard deviation level (96% probability) for E(θ,Ω,z) are indicated with an *. For a number of sites, E(θ,Ω,z) can show significant change even when there is almost no change in Ω, where the change in E(θ,Ω,z) is caused by increases or decreases in C_T. The expected change in E_O(θ,Ω,z) with ozone change ranges from about 0.82 to 1.2 (see R(θ) in Table A1 and Fig. A1) depending on the latitude (SZA as a function of latitude). Sites deviating significantly from this ratio have been affected by changes in cloud transmission.

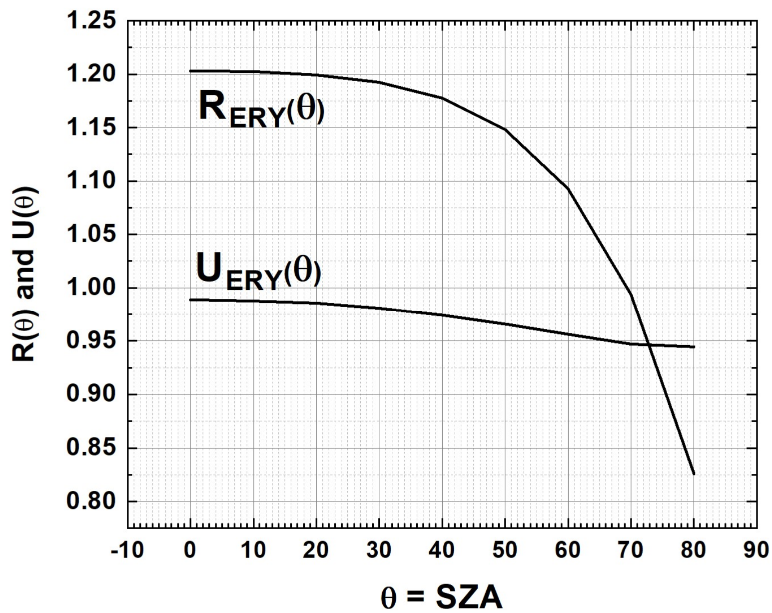

Fig. A1 Values of the coefficients $R_{ERY}(\theta)$ and $U_{ERY}(\theta)$

https://doi.org/10.5194/acp-2019-793
Preprint. Discussion started: 21 October 2019

A similar approximate analysis can be obtained for height dependence of other action spectra given by Herman (2010) for Z_{km} = 0 and the references therein.

Table A3 Height Dependence of Six Action Spectra

Action Spectrum	Approximate Height Dependence
Vitamin-D VIT	$1 + 0.055\ Z_{km}$
Cataracts CAT	$1 + 0.050\ Z_{km}$
DNA Damage DNA	$1 + 0.056\ Z_{km}$
Erythemal ERY	$1 + 0.047\ Z_{km}$
Plant damage PLC	$1 + 0.046\ Z_{km}$
Plant Damage PLA	$1 + 0.038\ Z_{km}$

Height dependence increases for those action spectra with more emphasis on shorter UV wavelengths

Table A4 lists 105 city or land locations in various countries as indicated in alphabetical order.

Table A4 Erythemal UV Index and Linear Change for UVI, O_3, and Transmission 2005 – 2018 for 105 locations

Location	Lat	Lon	Alt	UVI	UVI	←---------------- Trends (%/Year) -----------------→					
	Deg	Deg	km	Avg	Max	Ery	±σ	Ozone	±σ	Trans	±σ
Abu Dhabi AE*	-24.47	54.37	0.01	8	14	-0.17	0.08	0.16	0.01	0.11	0.04
Abuja, HG	9.07	7.49	0.01	10	13	-0.5	0.05	0.09	0.01	-0.34	0.05
Accra GH	5.56	-0.19	0.03	10	13	-0.05	0.05	0.14	0.01	0.12	0.04
Adelaide, AU*	-34.92	138.6	0	6	13	-0.45	0.14	0.17	0.02	-0.18	0.05
Albuquerque, NM	35.1	-106.6	1.58	6	12	0.18	0.11	-0.11	0.02	0.33	0.05
Algiers DZ	36.75	3.04	0.19	5	10	0.23	0.13	-0.08	0.02	0.37	0.05
Alice Springs, AU*	-23.7	133.88	0.58	9	15	-0.29	0.08	0.11	0.01	-0.12	0.04
Anchorage, AK	61.1	-149.9	0.03	2	6	0.37	0.2	-0.33	0.03	0.63	0.08
Athens, GR	37.98	23.73	0.72	5	11	0.02	0.14	-0.07	0.02	0.26	0.05
Atlanta, GA	33.5	-84.5	0.31	6	11	-0.2	0.12	-0.1	0.02	-0.41	0.07
Auckland, NZ	-36.85	174.76	0.05	5	13	0.02	0.14	0.22	0.02	0.16	0.06
Bangalore, IN*	12.97	77.58	0.91	10	14	-0.21	0.05	0.14	0.01	0.03	0.05
Bangkok TH*	13.74	100.52	0.01	9	13	-0.25	0.05	0.14	0.01	-0.01	0.04
Bangor, ME	44.81	-68.8	0.05	3	9	-0.17	0.17	-0.13	0.03	-0.08	0.08
Beijing, CN	39.9	116.4	0.05	4	9	0.25	0.13	-0.1	0.02	0.04	0.06
Bogota CO*	4.62	-74.06	2.54	10	15	-0.73	0.05	0.21	0.01	-0.43	0.05
Boston, MA*	42.36	-71.05	0.04	4	9	0.76	0.16	-0.13	0.03	0.62	0.08
Brasilia, BR*	-15.83	-47.93	1.17	10	15	0.16	0.06	0.12	0.01	0.22	0.05
Brisbane AU	-27.47	153.03	0.03	8	14	-0.18	0.1	0.14	0.02	0.01	0.05
Buenos Aires, AR	-34.6	-58.4	0.03	6	13	-0.15	0.14	0.08	0.02	-0.1	0.07
Bulawayo, ZW	-20.15	28.58	1.35	9	15	0.13	0.07	0.13	0.01	0.23	0.05
Canberra, AU*	-35.28	149.13	0.57	6	13	-0.41	0.13	0.17	0.02	-0.27	0.06
Cape Town ZA*	-33.92	18.42	0.04	7	13	-0.24	0.12	0.19	0.02	-0.02	0.04
Caracas, VZ*	10.5	-66.92	0.9	11	14	-0.09	0.04	0.13	0.01	0.12	0.03
Casablanca MA	33.59	-7.6	0.15	6	11	0	0.11	-0.07	0.02	0.11	0.04

https://doi.org/10.5194/acp-2019-793
Preprint. Discussion started: 21 October 2019

Atmospheric Chemistry and Physics Discussions

Chennai, IN*	13.07	80.24	0.02	10	13	-0.41	0.05	0.12	0.01	-0.19	0.05
Chicago, US*	41.89	-87.67	0.19	4	10	-0.42	0.17	-0.04	0.03	-0.37	0.09
Christchurch, NZ	-43.53	172.64	0.02	4	11	-0.11	0.17	0.33	0.03	-0.1	0.07
Cordoba AR	-31.41	64.18	0.4	7	13	-0.15	0.12	0.21	0.02	0.12	0.05
Darwin, AU*	-12.5	120.8	0.01	11	14	0.04	0.05	0.12	0.01	0.15	0.04
Des Moines, IA	41.6	-93.6	0.29	4	10	0.01	0.17	-0.06	0.02	0.55	0.09
Detroit, MI	42.3	-83.05	0.19	4	9	0.21	0.17	-0.08	0.03	0.4	0.09
Dhaka, BD*	23.7	90.4	0.01	8	12	-0.47	0.07	0.14	0.01	-0.19	0.06
Dongguan CN	23.02	113.75	0.01	6	12	-0.45	0.09	0.06	0.02	-0.37	0.09
Eureka, CA*	40.8	-124.1	0.01	4	10	0.33	0.14	-0.08	0.03	0.4	0.06
Giza EG	30	31.21	0.03	7	11	-0.06	0.09	0.06	0.02	0.11	0.03
Greenbelt, MD	39	-76.9	0.06	4	10	-0.19	0.15	-0.13	0.03	-0.1	0.08
Hamilton, NZ*	-37.85	175.32	0.05	5	12	-0.31	0.15	0.25	0.03	-0.13	0.07
Hartford, CT	41.8	-72.8	0.01	4	9	0.12	0.16	-0.12	0.03	0.1	0.08
Helsinki, FI	61.92	25.75	0.01	2	6	-0.22	0.21	-0.06	0.03	-0.07	0.09
Honolulu, HI*	21.3	-157.8	0.01	9	12	-0.27	0.06	-0.02	0.01	-0.24	0.03
Iowa Center, IA	42	-93.5	0.3	4	10	0	0.17	-0.02	0.03	0.58	0.1
Iquitos, PE*	-3.75	-73.25	0.13	9	14	-0.41	0.06	0.14	0.01	-0.23	0.06
Jakarta, ID*	-6.21	106.85	0.08	9	13	-0.27	0.05	0.18	0.01	-0.04	0.06
Kinshasa, CD	-4.32	15.31	0.31	10	14	-0.08	0.05	0.17	0.01	0.13	0.05
La Quaca, AR*	-22.11	-65.57	4.46	12	18	-0.15	0.07	0.09	0.01	-0.12	0.04
Lagos, NG*	6.47	3.41	0.01	9	13	-0.44	0.07	0.1	0.01	-0.25	0.07
Lauder, NZ*	-45.05	169.7	0.37	4	11	0.43	0.18	0.31	0.03	0.26	0.07
La Paz, BO*	-16.5	-68.15	3.78	11	18	-0.46	0.05	0.14	0.01	-0.32	0.05
Leeds, UK*	53.8	-1.55	0.03	2	7	-0.43	0.2	0.09	0.03	-0.2	0.08
Lima PE*	-12.04	-77.03	0.15	10	15	-0.35	0.08	0.17	0.01	-0.2	0.05
London, UK	51.51	-0.12	0.02	2	7	0.12	0.19	0.04	0.03	0.01	0.08
Los Angeles, CA	34.5	-118.5	0.1	6	11	-0.06	0.11	-0.11	0.02	0.09	0.04
Madrid, ES	40.42	-3.7	0.65	5	10	-0.27	0.14	-0.07	0.02	-0.24	0.06
Makassar, ID*	-5.13	119.4	0.01	10	14	-0.27	0.06	0.19	0.01	-0.05	0.06
Manaus, BR	3.12	-60	0.09	11	14	-0.01	0.04	0.16	0.01	0.24	0.04
Manhattan, NY	40.76	-73.97	0.01	4	9	0.02	0.15	-0.19	0.03	-0.26	0.08
Marin County, CA	37.5	-122	0.1	6	11	0.04	0.12	-0.1	0.02	0.12	0.05
Mauna Loa Obs., HI*	19.54	155.6	3.4	11	15	-0.17	0.06	0.11	0.02	0.01	0.04
Melbourne, AU*	-37.3	145	0.01	5	13	-0.4	0.15	0.25	0.02	-0.24	0.06
Mendoza, AR*	-32.9	-68.9	0.83	7	14	-0.33	0.12	0.13	0.02	-0.12	0.04
Mexico City, MX*	19.43	-99.13	2.24	9	14	-0.26	0.06	0.07	0.01	-0.11	0.05
Moscow, RU*	55.75	37.62	0.15	2	7	0.47	0.22	-0.04	0.03	0.61	0.1
Mt_Everest_0	28	86.9	0	7	13	0	0.08	0.08	0.01	0.3	0.06
Mt_Everest_8.85	28	86.9	8.85	10	18	0	0.08	0.08	0.01	0.3	0.06
Mt. Kenya, KE*	0.13	37.3	5.2	14	18	-0.2	0.03	0.17	0.01	0.03	0.03
Mumbai, IN*	19.08	72.88	0.02	9	13	-0.14	0.06	0.12	0.01	0.04	0.05
Nairobi, KE*	1.09	35.88	1.86	12	15	-0.25	0.04	0.16	0.01	-0.04	0.03
New Delhi, IN	28.61	77.2	0.03	7	12	-0.06	0.08	0.11	0.01	0.09	0.04
Nice FR	43.67	7.29	0.03	4	9	0.01	0.15	-0.13	0.03	-0.05	0.06

https://doi.org/10.5194/acp-2019-793
Preprint. Discussion started: 21 October 2019

Palembang, ID*	-2.99	104.76	0.01	9	14	-0.27	0.06	0.2	0.01	0	0.06
Paris, FR*	48.86	2.35	0.04	3	8	0.47	0.18	-0.01	0.03	0.51	0.08
Perth, AU	-31.95	115.9	0.03	7	14	-0.03	0.12	0.21	0.02	0.22	0.04
Pilar, AR	-31.66	-63.88	0.34	7	14	-0.02	0.12	0.07	0.02	-0.09	0.06
Punta Arenas, CL	-53.16	-70.92	0.04	3	9	-0.15	0.2	0.17	0.02	-0.15	0.07
Queenstown, SÁ	-31.9	26.92	1.1	7	14	-0.12	0.11	0.16	0.01	0.01	0.05
Quezon City PH	14.65	121.05	0.05	8	13	-0.12	0.07	0.2	0.01	0.21	0.06
Quito, EC	0.18	-78.5	2.85	7	12	0.05	0.05	0.17	0.01	0.28	0.05
Reading, CA	40.5	-122.4	0.03	5	10	0.2	0.14	-0.02	0.03	0.3	0.06
Recife, BR	-8.05	-34.93	0.55	11	14	-0.08	0.05	0.14	0.01	0.13	0.03
Rio de Janeiro BR	-22.9	-43.21	0	8	14	0.19	0.1	0.17	0.01	0.15	0.07
Riyadh, SÁ*	24.77	46.68	0.62	9	13	-0.17	0.07	0.09	0.01	0.03	0.03
Rome, IT	41.9	12.5	0.01	4	10	0.13	0.15	-0.16	0.02	0.3	0.06
Rosario, AR*	-32.94	-60.64	0.03	6	14	-0.3	0.13	0.08	0.02	-0.26	0.06
Rural Georgia, GA*	34.5	-83.5	0.2	5	10	0.3	0.12	-0.08	0.02	0.15	0.07
Sacramento, CA	38.5	-121.5	0.08	5	10	0	0.13	-0.09	0.02	0.15	0.05
Salt Lake, City UT	40.7	-111.9	1.32	5	11	0.24	0.16	-0.08	0.02	0.48	0.07
San Julian, AR	-49.32	-67.75	0.06	3	10	0.14	0.18	0.16	0.02	0.13	0.06
Santa Rosa, CA	38.5	-122.7	0.05	5	10	0.12	0.13	-0.09	0.02	0.19	0.05
Santiago CL	-33.46	-70.65	0.56	7	14	-0.06	0.15	0.17	0.02	0.39	0.08
San Jose, CA	37.5	-122.5	0.14	5	10	0.23	0.12	-0.1	0.02	0.31	0.05
San Pedro, CL	-22.9	-68.2	2.45	11	17	-0.04	0.08	0.15	0.01	0.06	0.02
Seattle, WA	47.5	-123.5	0.14	3	9	0.3	0.19	-0.09	0.03	0.29	0.09
Shanghai, CN*	31.22	121.47	0.06	5	11	-0.32	0.13	-0.02	0.02	-0.27	0.09
Stanley FK	-51.7	-57.9	0.05	3	9	0.18	0.19	0.12	0.02	0.15	0.07
Tampa, FL*	28	-82.5	0.01	7	11	-0.24	0.09	-0.03	0.02	-0.25	0.06
Tel Aviv, IL	32.11	34.86	0.03	7	11	-0.12	0.11	-0.01	0.02	-0.01	0.03
Tokyo JP*	35.65	139.84	0.04	4	10	0.42	0.13	0.05	0.02	0.52	0.08
Ushuaia, AR	-54.8	-68.3	0.06	2	8	0.01	0.2	0.18	0.03	0.05	0.07
Utah Center, UT	39	-109.5	1.8	5	11	-0.15	0.14	-0.1	0.02	0	0.06
Vientiane, LA	17.97	102.63	0.17	9	12	-0.03	0.05	0.11	0.01	0.12	0.05
Wellington NZ	-41.3	174.8	0.08	5	12	-0.6	0.16	0.31	0.03	-0.35	0.06
White Sands, NM	32.4	-106.5	1.22	7	12	-0.07	0.1	-0.07	0.02	-0.06	0.04

ΔE is the slope S ± σ of the linear least squares fit to the time series E(t) with 1 standard deviation σ
<E> is the average value of E(t) for 2005 < t < 2018. * indicates significant 2σ change in E(t).
The same notation applies to the ozone time series O_3(t) and transmission T(t).

Two independent methods, Uniform Temporal Distribution UTD and Multivariate MV (Guttman, 1982), were used to calculate LS linear trends and their uncertainties ±σ showing that the methods yielded similar results (Table A5)

https://doi.org/10.5194/acp-2019-793
Preprint. Discussion started: 21 October 2019

Atmospheric Chemistry and Physics Discussions

Table A5 Comparison of UTD and MV methods of trend and uncertainty estimation

Location	Method	E(t) Trend (%/yr)	±σ (%/yr)	TO_3(t) Trend (%/yr)	±σ (%/yr)
Greenbelt, MD	MV	-0.22	0.22	-0.14	0.04
(ϕ = 39.0°)	UTD	-0.19	0.15	-0.13	0.03
Rural Georgia, GA	MV	0.27	0.19	-0.09	0.03
(ϕ = 34.5°)	UTD	0.30	0.12	-0.08	0.02
Buenos Aires, AR	MV	-0.15	0.21	0.07	0.03
(ϕ = -34.6°)	UTD	-0.20	0.14	0.08	0.02
Melbourne, AU	MV	-0.36	0.23	0.25	0.04
(ϕ = -37.5°)	UTD	-0.40	0.15	0.25	0.02
Ushuaia, AR	MV	0.02	0.31	0.18	0.04
(ϕ = -54.8°)	UTD	0.01	0.20	0.18	0.03

https://doi.org/10.5194/acp-2019-793
Preprint. Discussion started: 21 October 2019

5.0 References

Abraham, Alison G., Christopher Cox, Sheila West, The Differential Effect of Ultraviolet Light Exposure on Cataract Rate across Regions of the Lens, Investigative Ophthalmology & Visual Science August, Vol.51, 3919-3923. doi:10.1167/iovs.09-4557, 2010.

Akima, Hiroshi, A new method of interpolation and smooth curve fitting based on local procedures, J. ACM, 17(4), 589-602, 1970

Ambach, W. and Blumthaler, M., Biological effectiveness of solar UV radiation in humans, Experientia, 49: 747. https://doi.org/10.1007/BF01923543, 1993.

Australian Institute of Health and Welfare, Skin cancer in Australia. Cat. no. CAN 96. Canberra: AIHW, 2016.

Cede, Alexander, Luccini, Eduardo, Núñez, Liliana, Piacentini, Rubén, Blumthaler, Mario, Monitoring of erythemal irradiance in the Argentine ultraviolet network. Journal of Geophysical Research. 107. 10.1029/2001JD001206, 2002.

Cede, Alexander, Luccini, Eduardo, Núñez, Liliana, Piacentini, Rubén, Blumthaler, Mario, Herman, Jay, TOMS-derived erythemal irradiance versus measurements at the stations of the Argentine UV Monitoring Network. Journal of Geophysical Research. 109. 10.1029/2004JD004519, 2004.

Cleveland, William S., *LOWESS*: A program for smoothing scatterplots by robust locally weighted regression. The American Statistician. ***35** (1): 54.* JSTOR 2683591. doi:10.2307/2683591*, 1981.*

Diffey BL, Analysis of the risk of skin cancer from sunlight and solaria in subjects living in northern Europe, Photo-dermatology, 4(3):118-126], 1987.

Diffey BL. Time and place as modifiers of personal UV exposure. Int J Environ Res Public Health, 15(6):E1112, doi: 10.3390/ijerph15061112, 2018.

Findlay, G. M., Ultra-Violet Light and Skin Cancer. Lancet pp.1070-73 ref.14, 1928.

Guttman, I., Linear Models, An Introduction, 358 pp., Wiley-Interscience, New York, 1982.

Krotkov, N. A., J. R. Herman, P. K. Bhartia, V. Fioletov, and Z. Ahmad, Satellite estimation of spectral surface UV irradiance, 2. Effects of homogeneous clouds and snow, J. Geophys. Res., 106, 11,743–11,759, 2001.

Herman, J.R. and E Celarier, J. Geophys. Earth surface reflectivity climatology at 340-380 nm from TOMS data, 102, 28003-28011, 1997.

Herman, J.R., N. Krotkov, E. Celarier, D. Larko, and G. Labow, Distribution of UV radiation at the Earth's surface from TOMS-measured UV-backscattered radiances, J. Geophys. Res., 104, D10, 12,059–12,076, 1999.

https://doi.org/10.5194/acp-2019-793
Preprint. Discussion started: 21 October 2019

Atmospheric Chemistry and Physics Discussions
Open Access

Herman, J.R., G. Labow, N.C. Hsu, D. Larko, Changes in Cloud Cover (1998-2006) Derived From Reflectivity Time Series Using SeaWiFS, N7-TOMS, EP-TOMS, SBUV-2, and OMI Radiance Data, J. Geophys. Res., 114, D01201, doi:10.1029/2007JD009508, 2009.

Herman, J.R., Use of an improved radiation amplification factor to estimate the effect of total ozone changes on action spectrum weighted irradiances and an instrument response function, J. Geophys. Res., D23119, doi:10.1029/2010JD014317, 2010

Herman, J., Huang, L., McPeters, R., Ziemke, J., Cede, A., and Blank, K.: Synoptic ozone, cloud reflectivity, and erythemal irradiance from sunrise to sunset for the whole Earth as viewed by the DSCOVR spacecraft from the Earth–sun Lagrange 1 orbit, Atmos. Meas. Tech., 11, 177-194, https://doi.org/10.5194/amt-11-177-2018, 2018.

Howlader N, Noone AM, Krapcho M, Miller D, Brest A, Yu M, Ruhl J, Tatalovich Z, Mariotto A, Lewis DR, Chen HS, Feuer EJ, Cronin KA (eds). SEER Cancer Statistics Review, 1975-2016, National Cancer Institute. Bethesda, MD, https://seer.cancer.gov/csr/1975_2016/, based on November 2018 SEER data submission, posted to the SEER web site, April 2019.

Italia, Nadia, Eva A. Rehfuess, Is the Global Solar UV Index an effective instrument for promoting sun protection? A systematic review, *Health Education Research*, Volume 27, Issue 2, Pages 200–213, https://doi.org/10.1093/her/cyr050, 2012

Levelt, P. F., Joiner, J., Tamminen, J., Veefkind, J. P., Bhartia, P. K., Stein Zweers, D. C., Duncan, B. N., Streets, D. G., Eskes, H., van der A, R., McLinden, C., Fioletov, V., Carn, S., de Laat, J., DeLand, M., Marchenko, S., McPeters, R., Ziemke, J., Fu, D., Liu, X., Pickering, K., Apituley, A., González Abad, G., Arola, A., Boersma, F., Chan Miller, C., Chance, K., de Graaf, M., Hakkarainen, J., Hassinen, S., Ialongo, I., Kleipool, Q., Krotkov, N., Li, C., Lamsal, L., Newman, P., Nowlan, C., Suleiman, R., Tilstra, L. G., Torres, O., Wang, H., and Wargan, K.: The Ozone Monitoring Instrument: overview of 14 years in space, Atmos. Chem. Phys., 18, 5699-5745, https://doi.org/10.5194/acp-18-5699-2018, 2018.

Madronich, S. , The atmosphere and UV-B radiation at ground level, in Environmental UV Photobiology, edited by L. O. Björn, and A. R. Young, pp. 1–39, Plenum, New York, 1993a

Madronich, S. , UV radiation in the natural and perturbed atmosphere, in Environmental Effects of UV (Ultraviolet) Radiation, edited by M. Tevini, pp. 17–69, A. F. Lewis, Boca Raton, 1993b.

Madronich, S., and S. Flocke , Theoretical estimation of biologically effective UV radiation at the Earth's surface, in Solar Ultraviolet Radiation—Modeling, Measurements and Effects, NATO ASI Series,vol. I52, edited by C. Zerefos, Springer, Berlin, 1997.

McKinlay, A., and B. L. Diffey, A reference action spectrum for ultraviolet-induced erythema in human skin; in Human Exposure to Ultraviolet Radiation: Risks and Regulations, Int. Congress Ser., edited by W. F. Passchier, and B. F. M. Bosnajakovic, pp. 83–87, Elsevier, Amsterdam, Netherlands, 1987.

https://doi.org/10.5194/acp-2019-793
Preprint. Discussion started: 21 October 2019

Pollack, A. McGrath, M. Henderson, J. Britt, H. Skin cancer by state and territory, Australian Family Physician, The Royal Australian College of General Practitioners (RACGP), 507, http://www.racgp.org.au/afp/2014/august/skin-cancer-by-state-and-territory, 2014.

Roberts, Joan, Ultraviolet Radiation as a Risk Factor for Cataract and Macular Degeneration, Eye & Contact Lens: Science & Clinical Practice. 37(4):246-249,DOI:10.1097/ICL.0b013e31821cbcc9, PMID: 21617534, 2011.

Sánchez-Pérez, J. F., Vicente-Agullo, D., Barberá, M., Castro-Rodríguez, E., and Cánovas, M., Relationship between ultraviolet index (UVI) and first-, second- and third-degree sunburn using the Probit methodology, Nature Scientific Reports, 9, 2045-2322, https://doi.org/10.1038/s41598-018-36850-x, 2019.

Schenkeveld, V. M. E. and Jaross, G. and Marchenko, S. and Haffner, D. and Kleipool, Q. L. and Rozemeijer, N. C. and Veefkind, J. P. and Levelt, P. F., In-flight performance of the Ozone Monitoring Instrument, Atmospheric Measurement Techniques, 10, 1957-1986, 2017.

Strom SS, Yamamura Y., Epidemiology of nonmelanoma skin cancer, Clinics in Plastic Surgery, 24(4):627-636,1997

Weber, Mark, Coldewey-Egbers, Melanie, Fioletov, Vitali, Frith, Stacey & Wild, Jeannette & P. Burrows, John & S. Long, Craig & Loyola, Diego, Total ozone trends from 1979 to 2016 derived from five merged observational datasets - the emergence into ozone recovery. Atmospheric Chemistry and Physics Discussions. 2017. 1-37. 10.5194/acp-2017-853, 2017.

https://doi.org/10.5194/acp-2019-793
Preprint. Discussion started: 21 October 2019

Atmospheric Chemistry and Physics Discussions

Figure Captions

Fig, 1A Erythemal Irradiance E(ζ,ϕ,z,t) at six selected sites from Table A1 distributed within the United States. The red line is the linear fit to each of the time series. Also listed are the 14-year UVI average maximum and average values (UVI = E/25) (See table 1)

Fig. 1B Two sites from Fig. 1A, Greenbelt, Maryland and Rural Georgia, with the effect of clouds removed (i.e., T=1)

Fig. 2A Latitudinal distribution of E(ζ) and its contributing factors, TC(O_3), T, and SZA for a line of longitude passing through San Francisco, CA.

Fig. 2B Global distribution of E(ζ,ϕ) from DSCOVR EPIC data on 30 June 2017 19:17 GMT when there were few clouds.

Fig. 2C Latitudinal distribution of E(ζ,ϕ,z,t) and its contributing factors, TC(O_3), T, and SZA for a line of longitude passing near Greenwich England

Fig. 2D Global distribution of E(ζ,ϕ) from DSCOVR EPIC data on 04 July 2017 12:08 GMT.

Fig. 3. Four sites locate close to the equator. Mt Kenya at 0.1^{O}S, Quito Ecuador 0.2^{O}N, Makassar Indonesia 5.1^{O}S, Manaus Brazil 3.1^{O}N. The blue lines are a Lowess(0.04) fit (approximately 6 month running average).

Fig. 4 Panel A: A two week running average of cloud-free E(ζ,ϕ,z,t) corresponding to the data in Fig. 3A for Quito Ecuador and Manaus Brazil showing the effect of height and a small difference in average ozone amount. Panel B: An expansion for one year (2005) of E(ζ,ϕ,z,t) estimates for Quito showing the double peak as a function of minimum SZA near the equinoxes in the absence of clouds that is masked when clouds are included. The blue line shows the 20 DU variation in ozone between March and September.

Fig. 5: Six sites in the Southern Hemisphere including estimates of the trends for E(ζ,ϕ,z,t), TC(O_3), and the atmospheric transmission T caused by clouds and haze. The TC(O_3) time series (blue) is shown for Ushuaia

Fig. 6A Latitudinal distribution of E(ζ,ϕ,z,t) and its contributing factors, TC(O_3), T, and SZA for a line of longitude passing near Sydney, Australia

Fig. 6B Global distribution of E(ζ,ϕ) from DSCOVR EPIC data on 31 December 2017 02:24:36 GMT.

https://doi.org/10.5194/acp-2019-793
Preprint. Discussion started: 21 October 2019

Fig. 7 Monthly average variation in E(ζ,ϕ,z,t) for six sites in both the Northern and southern Hemispheres. Solid lines are from data summarized in a World Health Organization study. https://www.who.int/uv/intersunprogramme/activities/uv_index/en/index3.html. The small numbers are the height on the histogram bars (W/m^2).

Fig. 8 EPIC derived ozone amount (upper left in DU: 100 to 500 DU) and reflectivity (LER upper right in percent or RU: 0 to 100) for 22 June 2017 at t_O = 06:13 GMT. Lower left: color image of the Earth showing clouds and land areas. The brighter clouds are optically thick and correspond to the higher values of the LER.

Fig.9 Erythemal irradiance E(ζ,ϕ,z,t) and UVI from sunrise to sunset for 21 June 2017 solstice. The three images are for different GMT. Upper left 22 June 2017 (06:22GMT). Upper Right 21 June 2017 (11:21 GMT) and Lower Left 21 June 2017 (19:00 GMT). The images correspond to the sub-solar points over different continents caused by the Earth's rotation (15^O per hour).

Fig. 10A E(ζ,ϕ,t_O) near the summit of Mt. Everest at an altitude of 8.85 km. Mean T=0.7

Fig. 10B Erythemal irradiance on 22 June 2017 near Mt. Everest within the Tibetan Plateau region (red color) in mW/m^2

Fig. 11A E(ζ,ϕ,t_O) and UVI from sunrise to sunset for 21 September 2017 equinox. The three images are for different GMT

Fig. 11B E and UVI from sunrise to sunset for 21 March 2017 equinox. The three images are for different GMT (05;33, 10:56, and 16:20).

Fig. 12 E(ζ,ϕ,t_O) and UVI from sunrise to sunset for 21 December 2017 solstice. The three images are for different GMT

Fig. 13A Longitudinal slices of E(ζ,ϕ,t_O) (units UVI) at 0.1^ON and 30.85^ON latitude shown by the dark horizontal bars. The EPIC E(ζ,ϕ,t_O) images are for 14 April 2016 t_O = 04:21 GMT centered at about 10^ON and 104^OE. Panels A and C show longitudinal slices of E(ζ,ϕ,t_O) and T(ζ,ϕ,t_O) for ζ = 0.1^ON and panels B and D for 30.85^ON. The solid lines in panels A and B represent the SZA.

Fig 13B EPIC color image for 14 April 2016 at 04:12:16 GMT showing the distribution of cloud cover and land corresponding to Fig. 13A

Fig 13C EPIC scene reflectivity LER for 14 April 2016 at 04:12:16 GMT

https://doi.org/10.5194/acp-2019-793
Preprint. Discussion started: 21 October 2019

Atmospheric Chemistry and Physics
Discussions

Fig. 14 Zonal Maximum UVI (Panel A), Zonal Average (Panel B) on 14 April 2016 at 04:21 GMT from EPIC including the effect of clouds and haze, as a function of latitude. Both the data points and an Akima spline fit are shown.

Fig. 15. Fourteen-year UVI Average and UVI Maximum from Table A4 for 105 sites. Solid curves are Akima spline fits to the individual site data points. There are 4 high altitude sites listed, San Pedro, Chile (2.45 km), La Paz, Bolivia (3.78 km), Mt Kenya, Kenya (5.2 km), and Mt Everest, Nepal and China (8.85 km).

Fig. 16 Least squares (LS) percent change per year for (A) Erythemal Irradiance, (B) Atmospheric Transmission, and (C) Column Ozone for the period 2005 – 2018 from OMI observations at 105 individual sites (see Table A4). The solar cycle and quasi-biennial oscillation effects have not been removed. Error bars are 1σ. Red curve is a Lowess(0.3) fit to the data.

Fig. 17: Similar to Fig. 16 but over the Atlantic (Longitude 32^{O}W) and the Pacific (179^{O}W) Oceans with one data point every 10^{O} of latitude.

Fig. 18 Similar to Fig. 16 but for land areas as indicated for longitudes 20^{O}E, 90OW, 60^{O}E, 120^{O}W

Fig. 19 Zonal average of change column ozone amount and in atmospheric transmission (%/Yr). The red line in Fig. 19B is a Lowess(0.5) fit showing the general trend as a function of latitude.

https://doi.org/10.5194/acp-2019-793
Preprint. Discussion started: 21 October 2019

Atmospheric Chemistry and Physics Discussions

6.0 Author Contributions

Jay Herman is responsible for all the text, figures, erythemal algorithm, and trend determinations

Liang Huang is responsible for deriving Lambert Equivalent Reflectivities for the OMI and EPIC instruments and ozone for the EPIC instrument. He is also responsible for the in-flight calibration of the EPIC instrument's UV channels.

Alexander Cede and Matthew Kowalski are responsible for the stray light correction, and "flat-fielding" of the EPIC CCD

Karin Blank is responsible for the ongoing improvements in geolocation and determining the correct exposure times for the EPIC instrument.

Jerald Ziemke is responsible for verifying the method of linear least-squares trend determination used to analyze the OMI time series data

Author List

Jay Herman[1] Alexander Cede[2] Liang Huang[3] Jerald Ziemke[5]

Matthew Kowalewski[2], Karin Blank[4]

[1]University of Maryland Baltimore County JCET, Baltimore, Maryland USA
Jay.r.herman@nasa.gov

[2]SciGlob Instruments and Services, Ellicott City, Maryland, USA
alexander.cede@luftblick.at
matthew.g.kowalewski@nasa.gov

[3]Science Systems and Applications, Lanham, Maryland, USA
liang-kang.huang@ssaihq.com

[4]NASA Goddard Space Flight Center, Greenbelt, Maryland USA
karin.b.blank@nasa.gov

[5]Morgan State University, GESTAR, Baltimore Maryland
jerald.r.ziemke@nasa.gov

7.0 Acknowledgements The authors would like to thank and acknowlege the support of the DSCOVR project and the OMI science team for the OMI satellite project for making OMI data freely available

https://doi.org/10.5194/acp-2019-793
Preprint. Discussion started: 21 October 2019

Atmospheric Chemistry and Physics
Open Access
EGU
Discussions

8.0 Figures

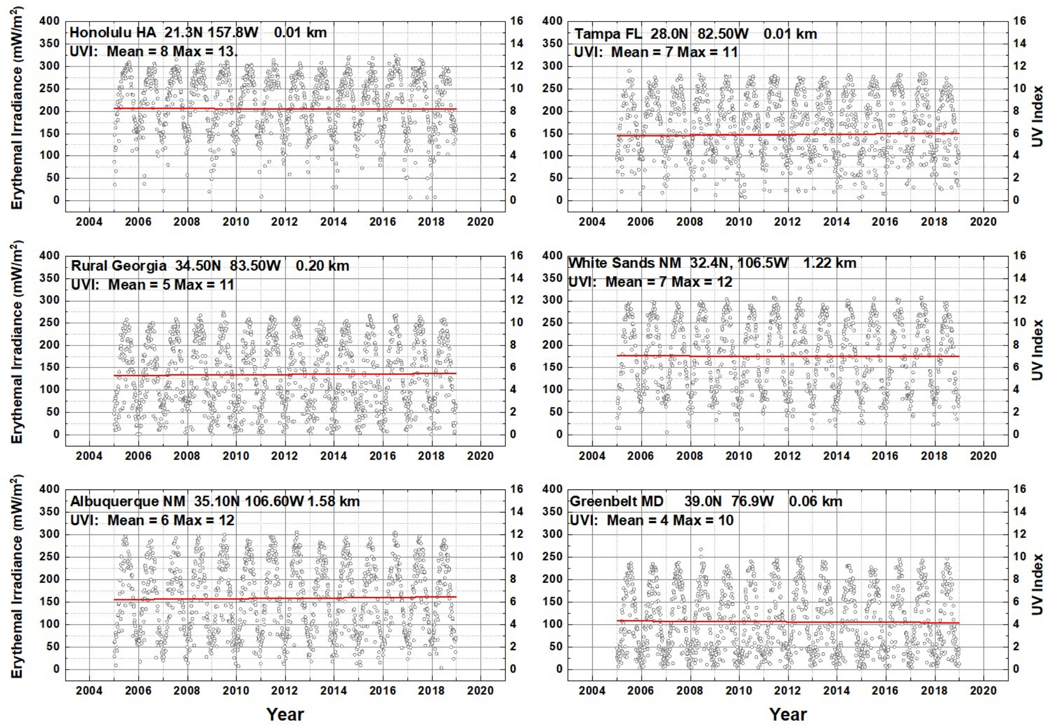

Fig. 1A Erythemal Irradiance E(ζ,ϕ,z,t) at six selected sites from Table A1 distributed within the United States. The red line is the linear fit to each of the time series. Also listed are the 14-year UVI average maximum and average values (UVI = E/25) (See table 1)

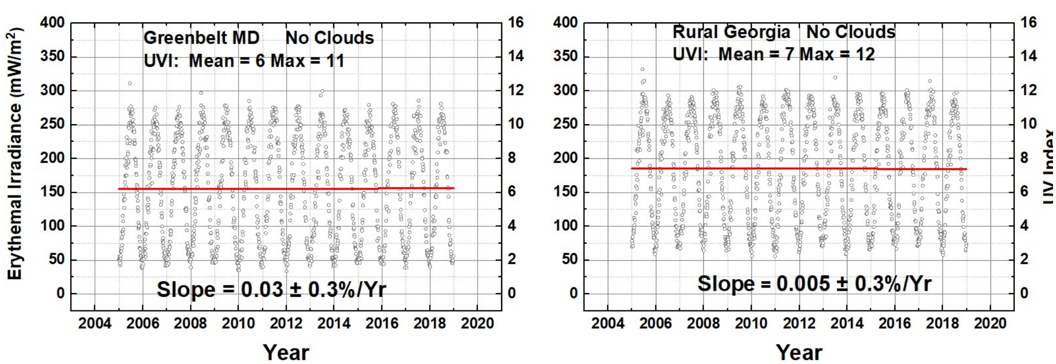

Fig. 1B Two sites from Fig. 1A, Greenbelt, Maryland and Rural Georgia, with the effect of clouds removed (i.e., T=1)

Figure 1A and Figure 1B

https://doi.org/10.5194/acp-2019-793
Preprint. Discussion started: 21 October 2019

Atmospheric Chemistry and Physics
Discussions

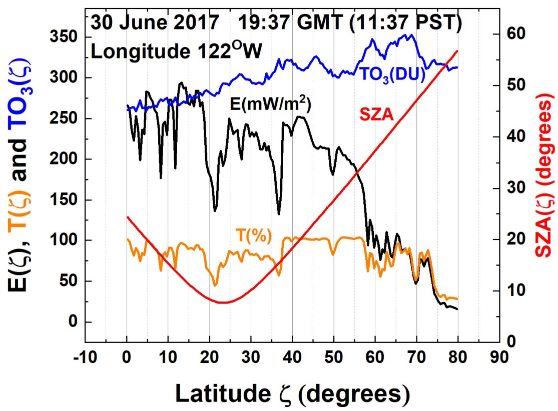

Fig. 2A Latitudinal distribution of E(ζ) and its contributing factors, TC(O_3), T, and SZA for a line of longitude passing through San Francisco, CA.

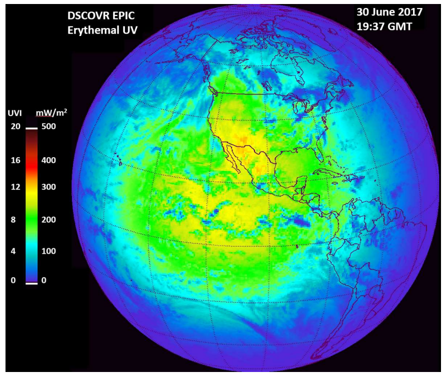

Fig. 2B Global distribution of E(ζ,ϕ) from DSCOVR EPIC data on 30 June 2017 19:17 GMT when there were few clouds.

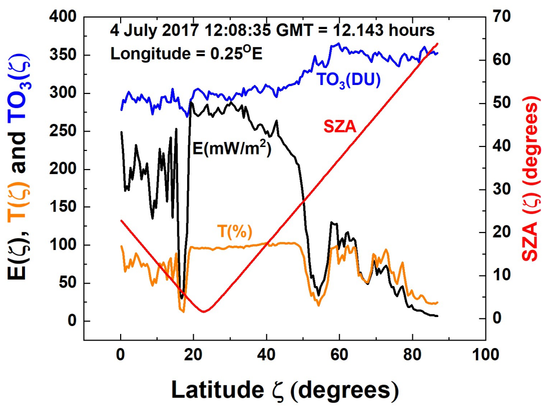

Fig. 2C Latitudinal distribution of E(ζ,ϕ,z,t) and its contributing factors, TC(O_3), T, and SZA for a line of longitude passing near Greenwich England

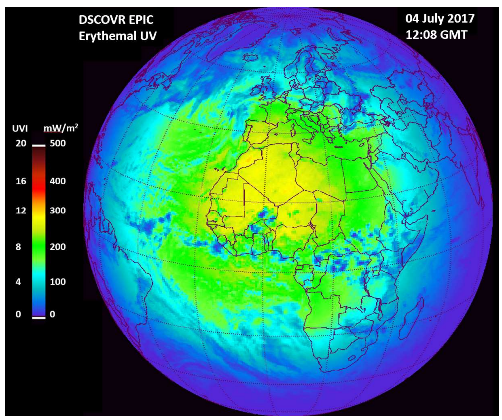

Fig. 2D Global distribution of E(ζ,ϕ) from DSCOVR EPIC data on 04 July 2017 12:08 GMT.

Figures 2A 2B 2C 2D

https://doi.org/10.5194/acp-2019-793
Preprint. Discussion started: 21 October 2019

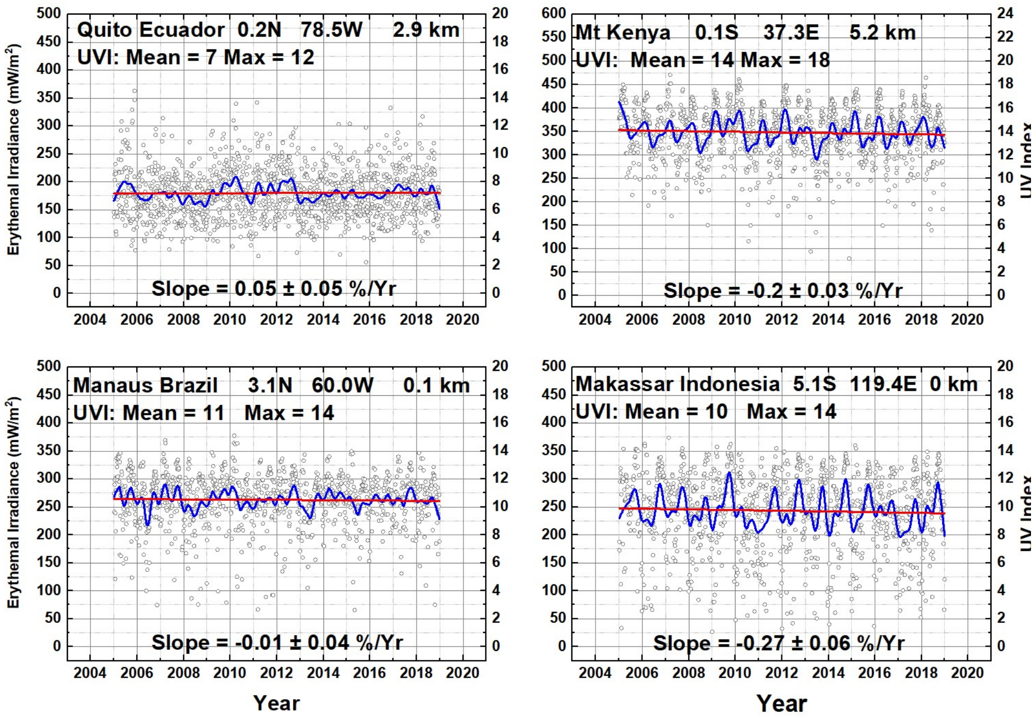

Fig. 3. Four sites locate close to the equator. Mt Kenya at 0.1^{O}S, Quito Ecuador 0.2^{O}N, Makassar Indonesia 5.1^{O}S, Manaus Brazil 3.1^{O}N. The blue lines are a Lowess(0.04) fit (approximately 6 month running average).

Figure 3

https://doi.org/10.5194/acp-2019-793
Preprint. Discussion started: 21 October 2019

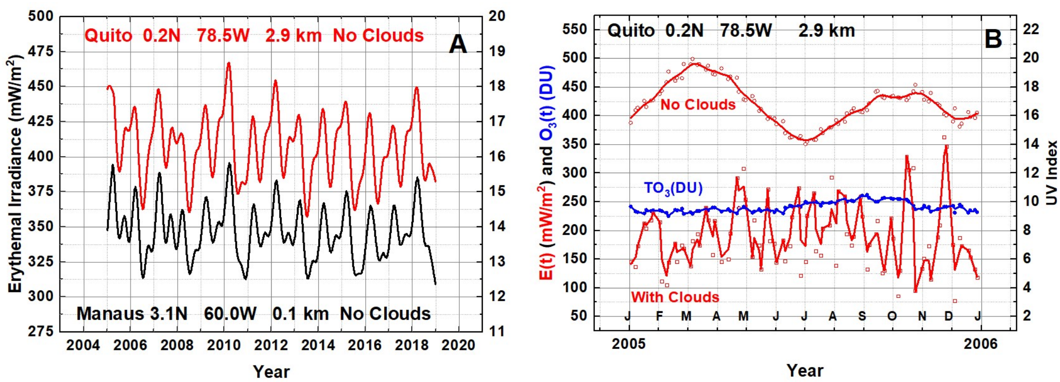

Fig. 4 Panel A: A two week running average of cloud-free E(ζ,ϕ,z,t) corresponding to the data in Fig. 3A for Quito Ecuador and Manaus Brazil showing the effect of height and a small difference in average ozone amount. Panel B: An expansion for one year (2005) of E(ζ,ϕ,z,t) estimates for Quito showing the double peak as a function of minimum SZA near the equinoxes in the absence of clouds that is masked when clouds are included. The blue line shows the 20 DU variation in ozone between March and September.

Figure 4

https://doi.org/10.5194/acp-2019-793
Preprint. Discussion started: 21 October 2019

Atmospheric Chemistry and Physics
Discussions

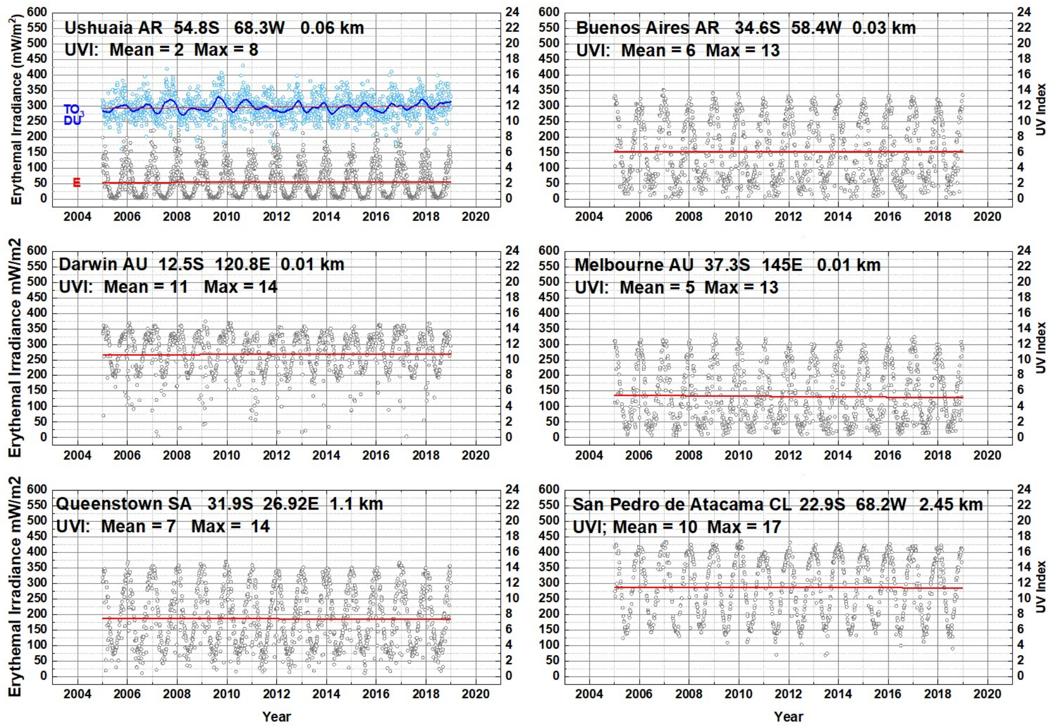

Fig. 5: Six sites in the Southern Hemisphere including estimates of the trends for E(ζ,ϕ,z,t), TC(O_3), and the atmospheric transmission T caused by clouds and haze. The TC(O_3) time series (blue) is shown for Ushuaia

Figure 5

https://doi.org/10.5194/acp-2019-793
Preprint. Discussion started: 21 October 2019

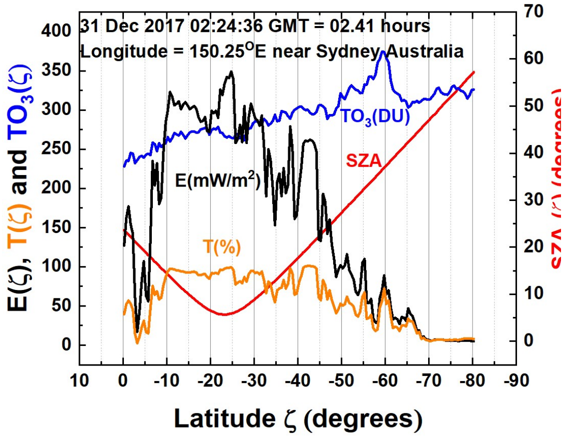

Fig. 6A Latitudinal distribution of E(ζ,ϕ,z,t) and its contributing factors, TC(O_3), T, and SZA for a line of longitude passing near Sydney, Australia

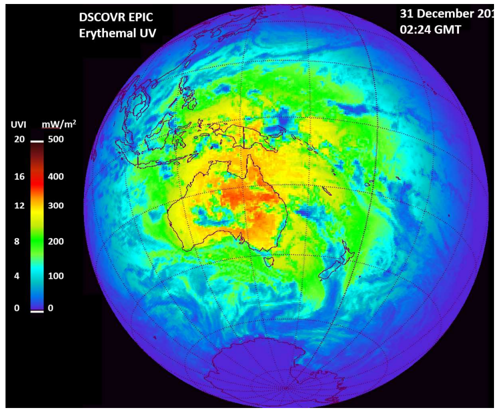

Fig. 6B Global distribution of E(ζ,ϕ) from DSCOVR EPIC data on 31 December 2017 02:24:36 GMT.

Figure 6A 6B

https://doi.org/10.5194/acp-2019-793
Preprint. Discussion started: 21 October 2019

Atmospheric Chemistry and Physics
Discussions

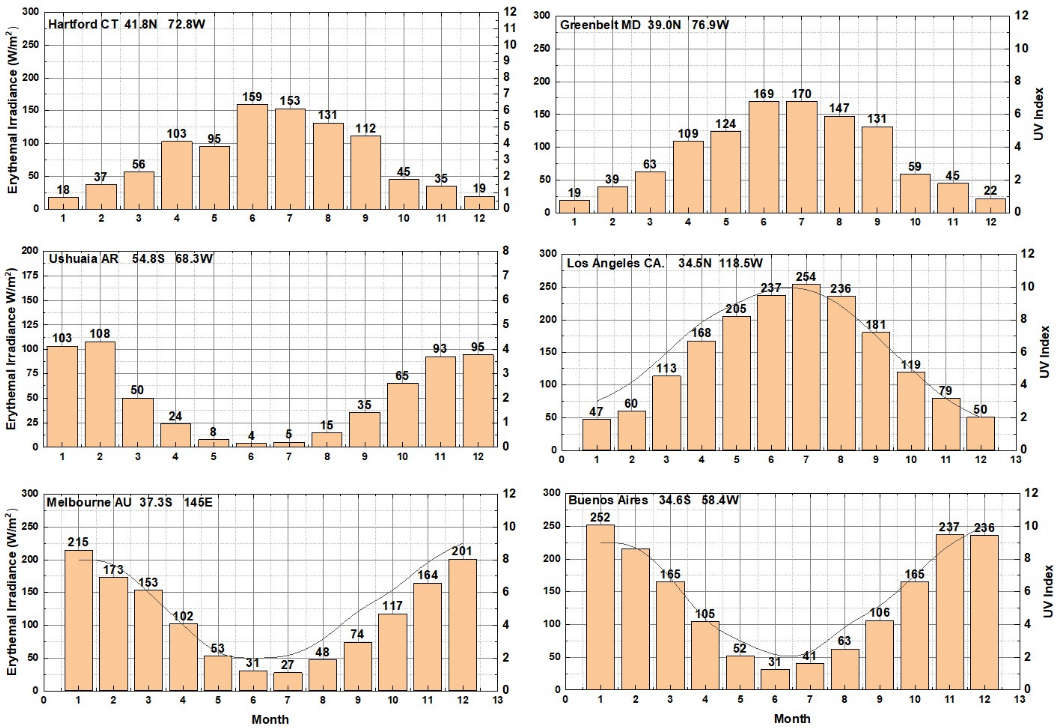

Fig. 7 Monthly average variation in E(ζ,ϕ,z,t) for six sites in both the Northern and southern Hemispheres. Solid lines are from data summarized in a World Health Organization study.

https://www.who.int/uv/intersunprogramme/activities/uv_index/en/index3.html. The small numbers are the height on the histogram bars (W/m^2).

Figure 7

https://doi.org/10.5194/acp-2019-793
Preprint. Discussion started: 21 October 2019

Atmospheric Chemistry and Physics Discussions
Open Access
EGU

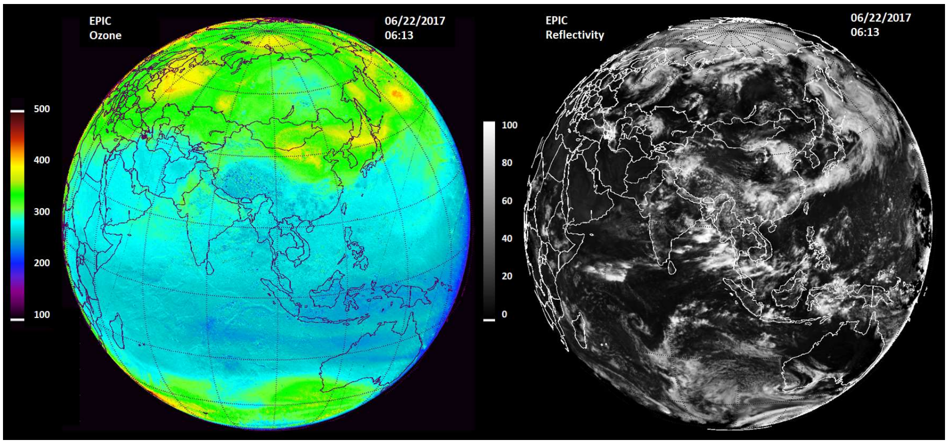

Fig. 8 EPIC derived ozone amount (upper left in DU: 100 to 500 DU) and reflectivity (LER upper right in percent or RU: 0 to 100) for 22 June 2017 at t_O = 06:13 GMT. Lower left: color image of the Earth showing clouds and land areas. The brighter clouds are optically thick and correspond to the higher values of the LER.

Figure 8

https://doi.org/10.5194/acp-2019-793
Preprint. Discussion started: 21 October 2019

Atmospheric Chemistry and Physics Discussions
Open Access
EGU

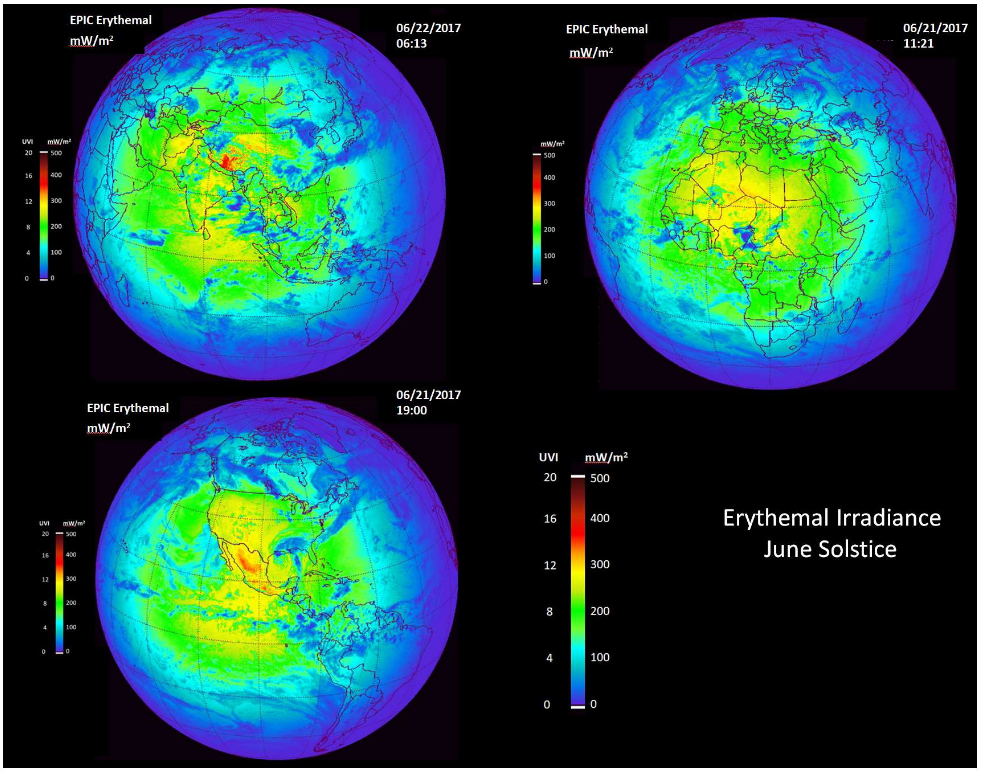

Fig.9 Erythemal irradiance E(ζ,ϕ,z,t) and UVI from sunrise to sunset for 21 June 2017 solstice. The three images are for different GMT. Upper left 22 June 2017 (06:22GMT). Upper Right 21 June 2017 (11:21 GMT) and Lower Left 21 June 2017 (19:00 GMT). The images correspond to the sub-solar points over different continents caused by the Earth's rotation (15^{O} per hour).

Figure 9

https://doi.org/10.5194/acp-2019-793
Preprint. Discussion started: 21 October 2019

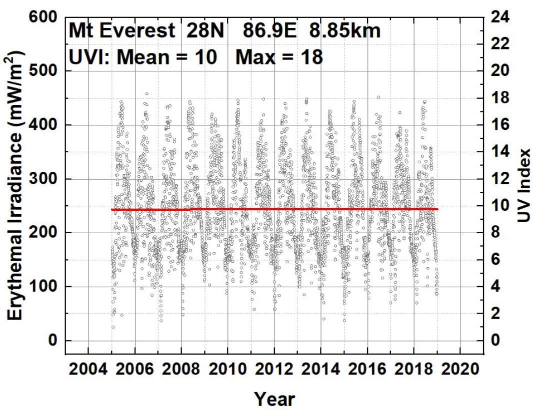

Fig. 10A $E(\zeta,\phi,t_O)$ near the summit of Mt. Everest at an altitude of 8.85 km. Mean T=0.7

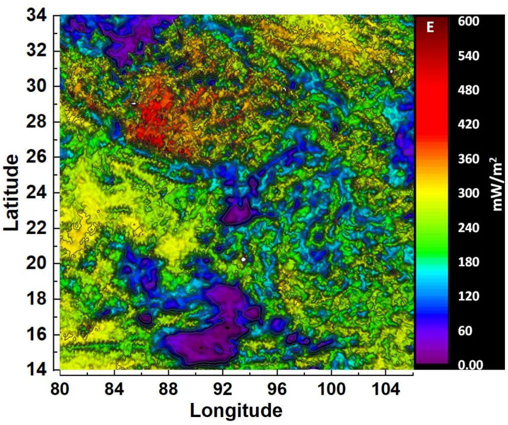

Fig. 10B Erythemal irradiance on 22 June 2017 near Mt. Everest within the Tibetan Plateau region (red color) in mW/m^2

Figures 10A 10B

Atmospheric Chemistry and Physics Discussions
Open Access
EGU

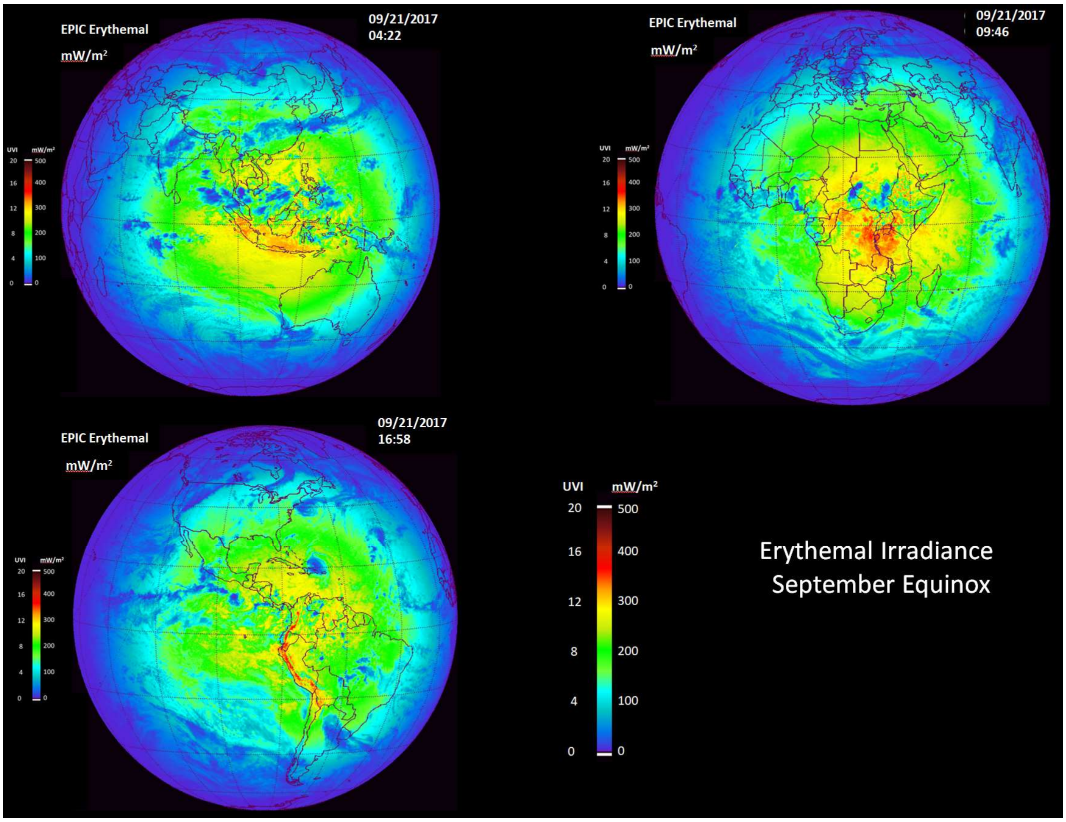

Fig. 11A E(ζ,ϕ,t_O) and UVI from sunrise to sunset for 21 September 2017 equinox. The three images are for different GMT

Figure 11A

https://doi.org/10.5194/acp-2019-793
Preprint. Discussion started: 21 October 2019

Atmospheric Chemistry and Physics Discussions

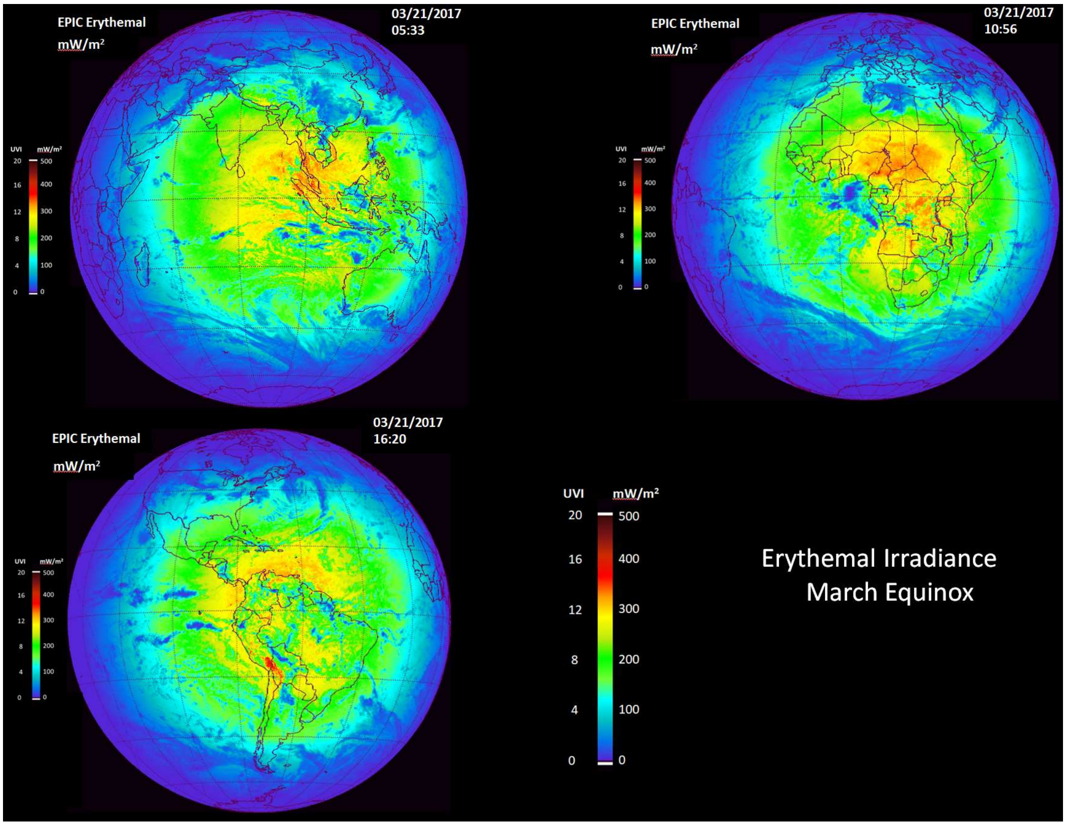

Fig. 11B E and UVI from sunrise to sunset for 21 March 2017 equinox. The three images are for different GMT (05;33, 10:56, and 16:20).

Figure 11B

https://doi.org/10.5194/acp-2019-793
Preprint. Discussion started: 21 October 2019

Atmospheric Chemistry and Physics Discussions

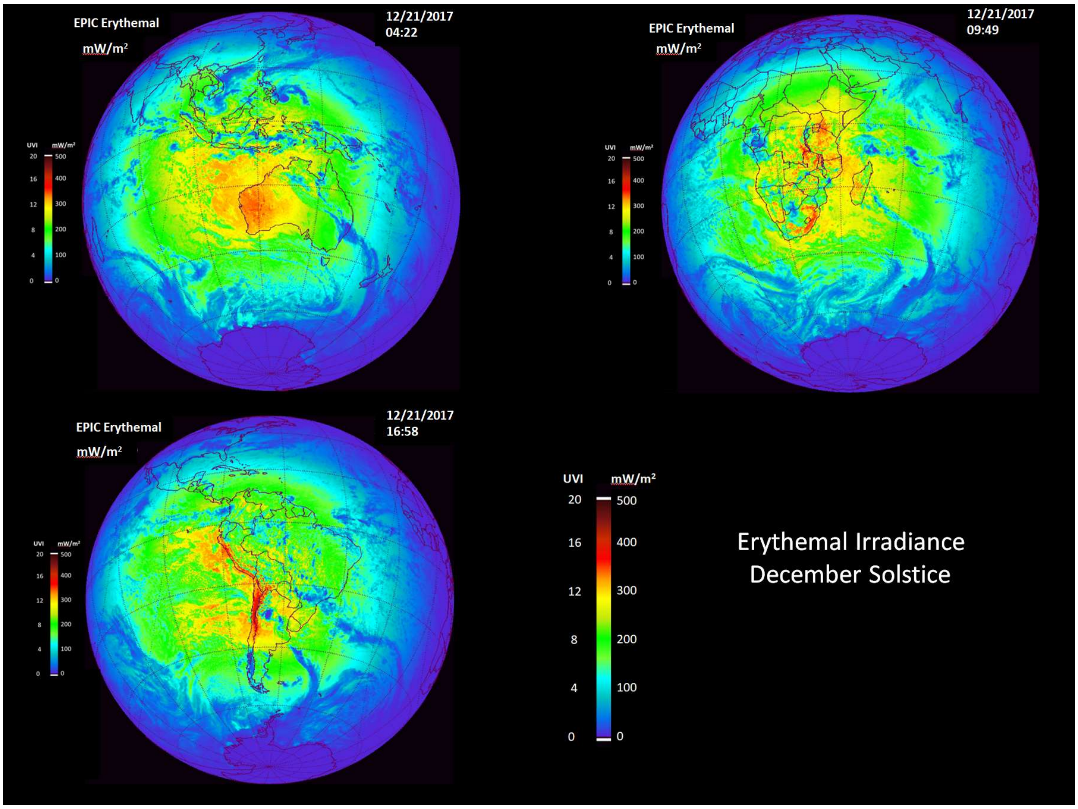

Fig. 12 E(ζ,ϕ,t_O) and UVI from sunrise to sunset for 21 December 2017 solstice. The three images are for different GMT.

Figure 12

https://doi.org/10.5194/acp-2019-793
Preprint. Discussion started: 21 October 2019

Atmospheric Chemistry and Physics
Open Access
Discussions

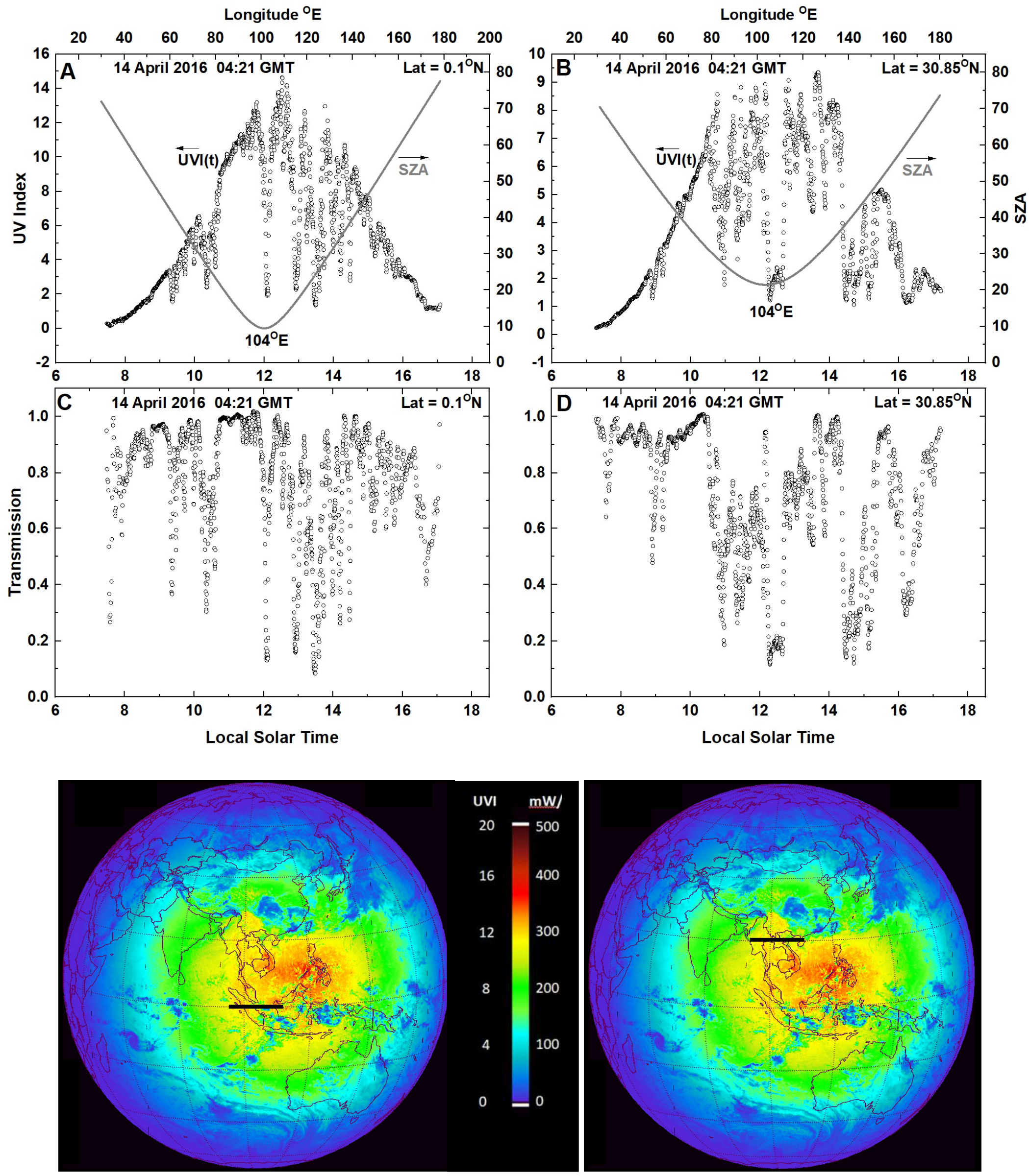

Fig. 13A Longitudinal slices of E(ζ,ϕ,t_O) (units UVI) at 0.1°N and 30.85°N latitude shown by the dark horizontal bars. The EPIC E(ζ,ϕ,t_O) images are for 14 April 2016 t_O = 04:21 GMT centered at about 10°N and 104°E. Panels A and C show longitudinal slices of E(ζ,ϕ,t_O) and T(ζ,ϕ,t_O) for ζ = 0.1°N and panels B and D for 30.85°N. The solid lines in panels A and B represent the SZA.

Figure 13A

https://doi.org/10.5194/acp-2019-793
Preprint. Discussion started: 21 October 2019

Atmospheric Chemistry and Physics Discussions
Open Access

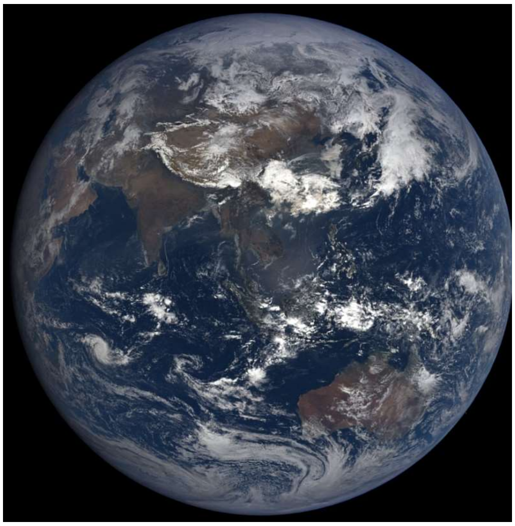

Fig 13B EPIC color image for 14 April 2016 at 04:12:16 GMT showing the distribution of cloud cover and land corresponding to Fig. 13A

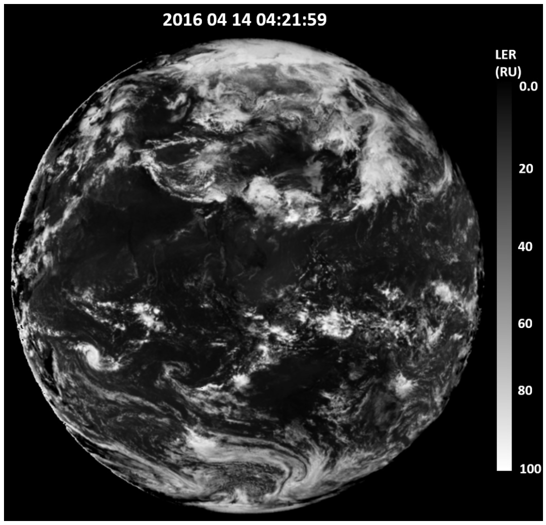

Fig 13C EPIC scene reflectivity LER for 14 April 2016 at 04:12:16 GMT

Figure 13B

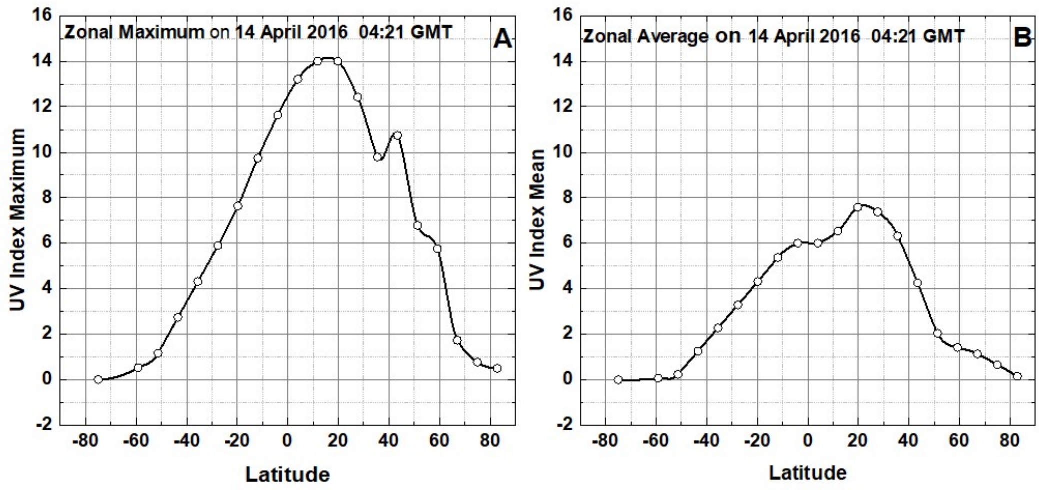

Fig. 14 Zonal Maximum UVI (Panel A), Zonal Average (Panel B) on 14 April 2016 at 04:21 GMT from EPIC including the effect of clouds and haze, as a function of latitude. Both the data points and an Akima spline fit (Akima, 1970) are shown.

Figure 14

https://doi.org/10.5194/acp-2019-793
Preprint. Discussion started: 21 October 2019

Atmospheric Chemistry and Physics
Open Access
Discussions

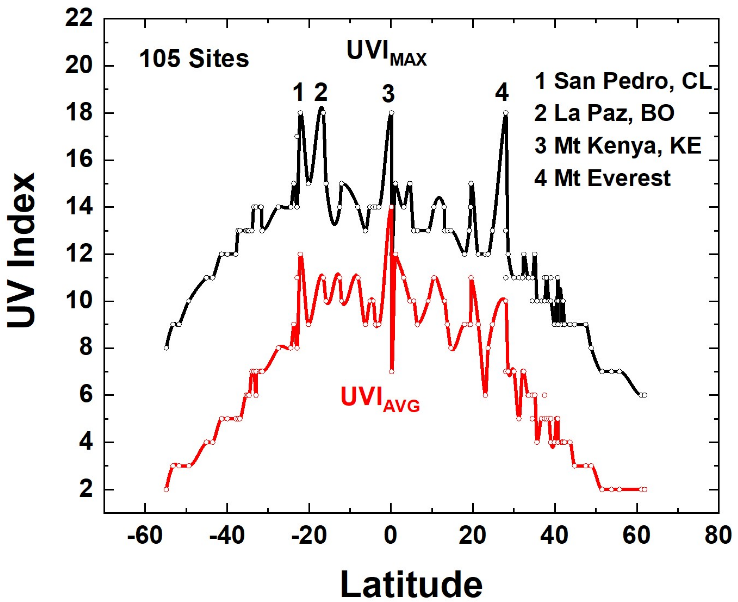

Fig. 15. Fourteen-year UVI Average and UVI Maximum from Table A4 for 105 sites. Solid curves are Akima spline fits (Akima, 1970) to the individual site data points. There are 4 high altitude sites listed, San Pedro, Chile (2.45 km), La Paz, Bolivia (3.78 km), Mt Kenya, Kenya (5.2 km), and Mt Everest, Nepal and China (8.85 km).

Figure 15

https://doi.org/10.5194/acp-2019-793
Preprint. Discussion started: 21 October 2019

Atmospheric Chemistry and Physics
Discussions

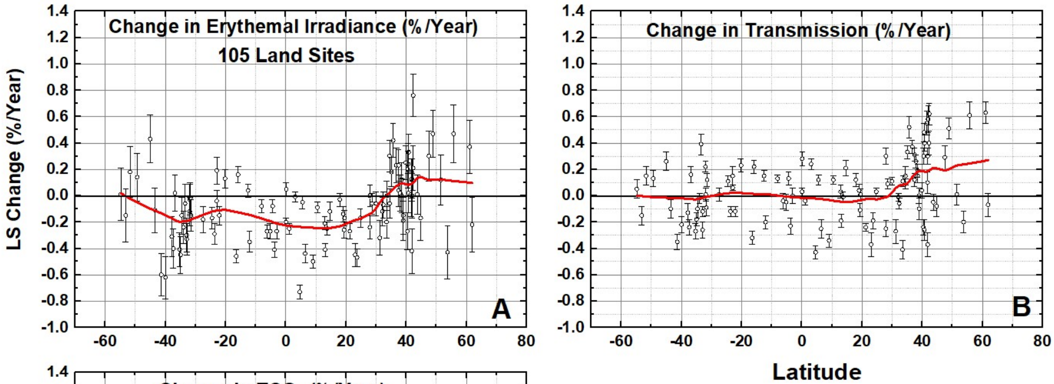

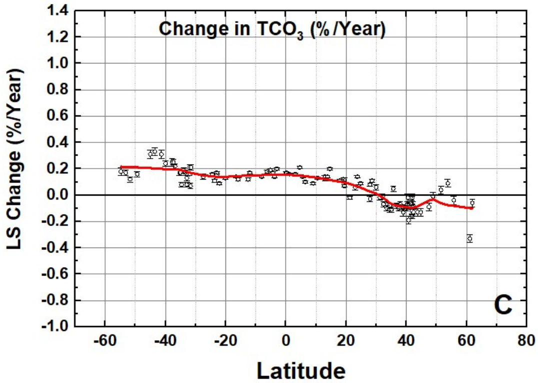

Fig. 16 Least squares (LS) percent change per year for (A) Erythemal irradiance, (B) Atmospheric Transmission, and (C) Column Ozone for the period 2005 – 2018 from OMI observations at 105 individual sites (see Table A4). The solar cycle and quasi-biennial oscillation effects have not been removed. Error bars are 1σ. Red curve is a Lowess(0.3) fit to the data.

Figure 16

https://doi.org/10.5194/acp-2019-793
Preprint. Discussion started: 21 October 2019

Atmospheric Chemistry and Physics Discussions

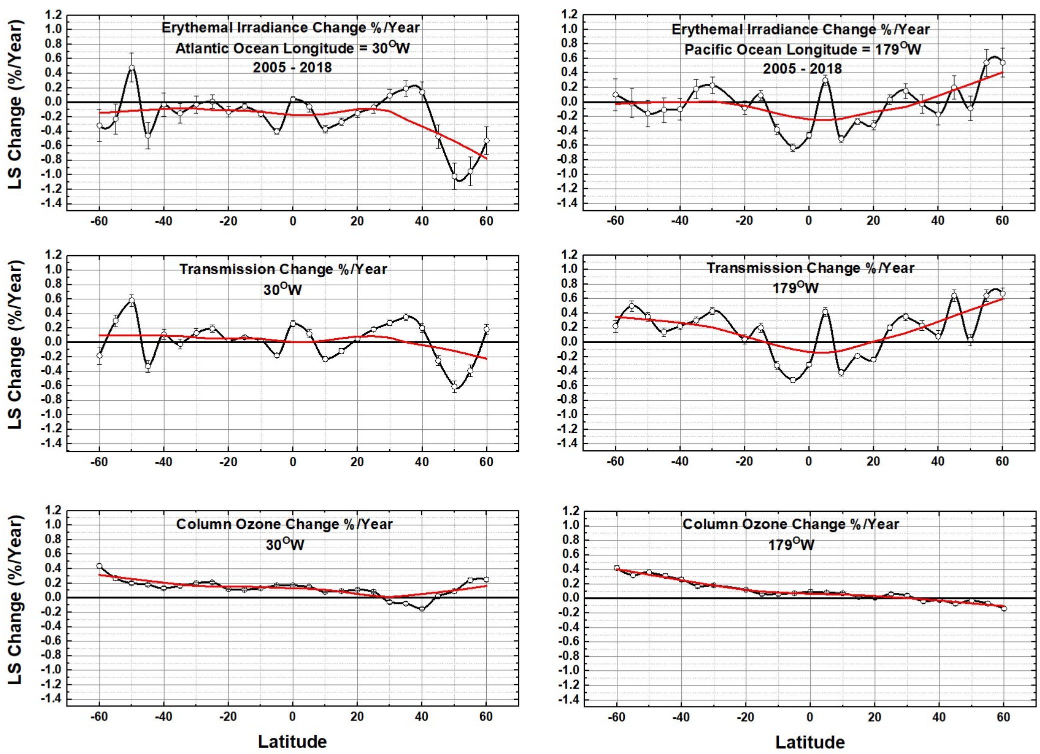

Fig. 17: Similar to Fig. 16 but over the Atlantic (Longitude 32°W) and the Pacific (179°W) Oceans with one data point every 10° of latitude.

989

990

991

992

993 **Figure 17**

994

https://doi.org/10.5194/acp-2019-793
Preprint. Discussion started: 21 October 2019

Atmospheric Chemistry and Physics
Open Access
Discussions

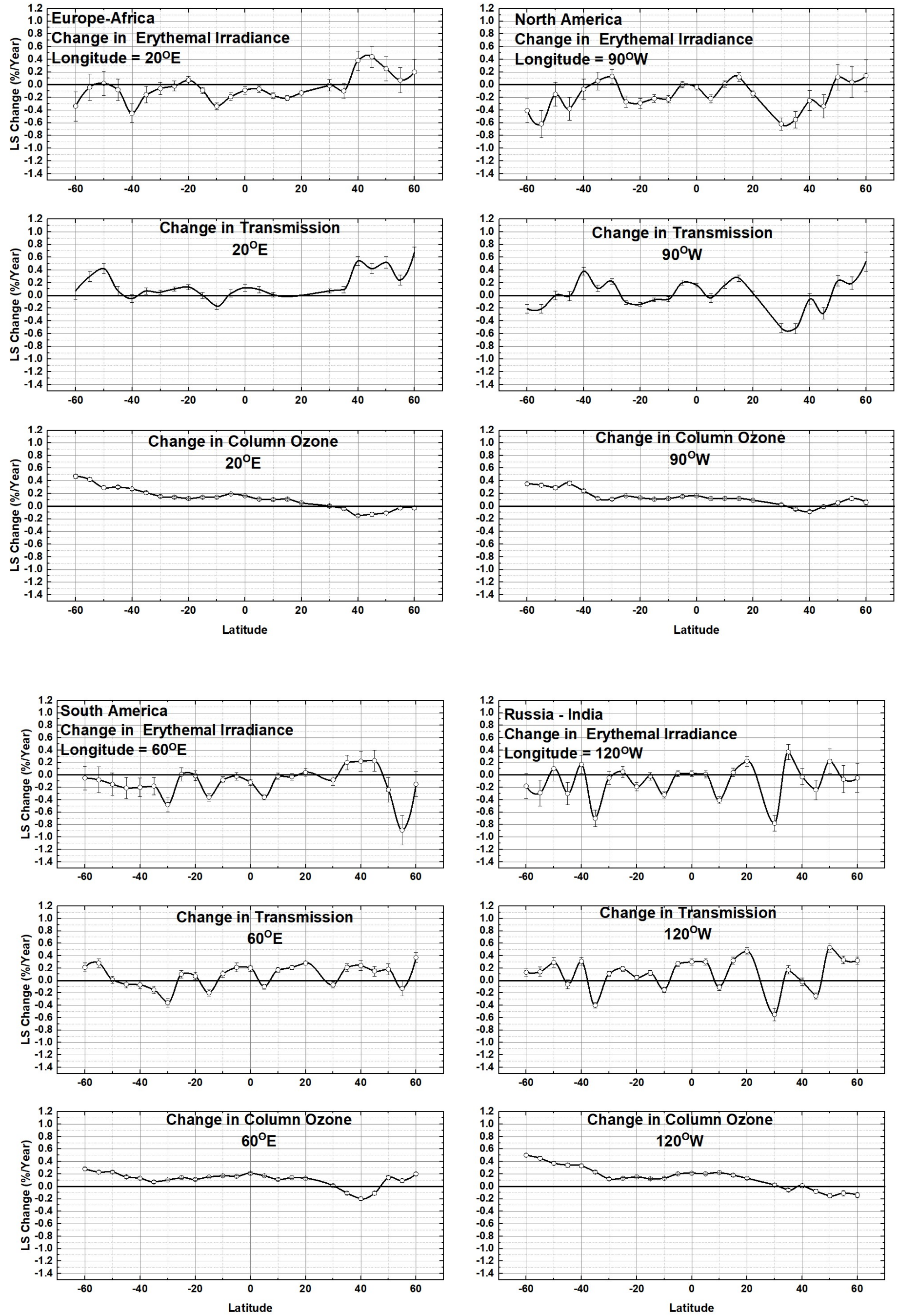

Fig. 18 Similar to Fig. 16 but for land areas as indicated for longitudes 20°E, 90OW, 60°E, 120°W

Figure 18

https://doi.org/10.5194/acp-2019-793
Preprint. Discussion started: 21 October 2019

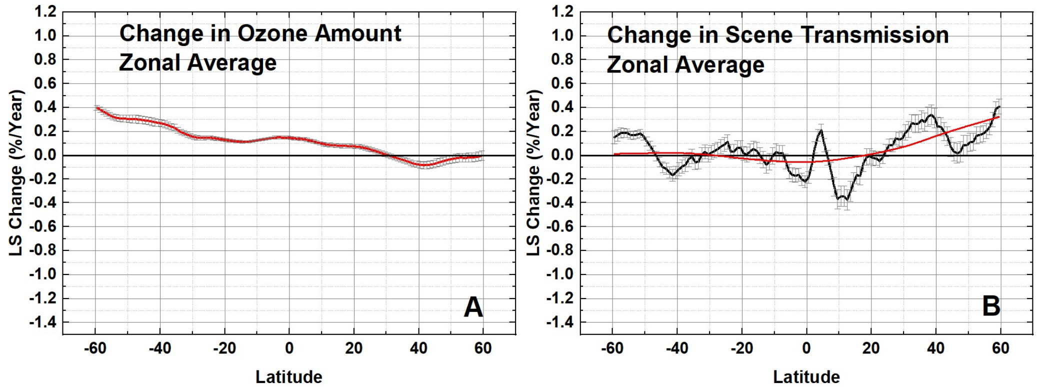

Fig. 19 Zonal average of change column ozone amount and in atmospheric transmission (%/Yr). The red line in Fig. 19B is a Lowess(0.5) fit showing the general trend as a function of latitude.

Figure 19